

Intense downwelling and diffuse upwelling in a Nonlinear Ekman Layer

Nikki Rahnamaei, Atmospheric and Ocean Sciences

McGill University, Montreal

DECEMBER, 2022

Supervised by Prof. David Straub

A thesis submitted to McGill University in partial fulfillment of the requirements

of the degree of

Master of Science

©Nikki Rahnamaei, DECEMBER 2022

Abstract

It has long been appreciated that Ekman transport and pumping velocities are modified through interactions with underlying geostrophic currents. Nonlinearity involving interaction of the Ekman flow with itself is, however, typically neglected. This occurs when the Rossby number based on the Ekman velocity and horizontal length scale approaches order one values. Such values are common, for example, in the ice-ocean stress field across sharp gradients such as leads in the sea ice cover. Recent work has shown strong asymmetry in the pumping velocities, with cyclonic forcing producing diffuse upwelling and anticyclonic forcing producing sharp downwelling fronts. To better understand this dynamics, we consider the steady response to a simple specified prescription of the stress. In the $(x-z)$ plane perpendicular to the stress, dynamics are described by the 2-d Navier-Stokes equation, with a forcing term dependent on vertical shear of velocity in the y -hat direction, specified by a pressureless momentum equation. An expansion in an Ekman-velocity based Rossby number is used to solve the system and to better understand the asymmetry. Interactions with stratification and underlying geostrophic currents are also considered, and examples of where these effects might be important are given. The self-advection of the Ekman flow is important in this asymmetrical phenomenon. As the asymmetry appears in the vorticity field, the self-advection of Ekman terms plays a stronger role in upwelling-downwelling asymmetry than the dissipative term. The solutions are found to be stable with significant noise added, however further research is needed to assess the more precise source of the asymmetry.

Abrégé

On sait depuis longtemps que le transport et la vitesse de pompage de l'Ekman sont modifiés par les interactions avec les courants géostrophiques sous-jacents. Cependant, la non-linéarité des interactions du l'écoulement d'Ekman avec lui-même est généralement négligée. Cela se produit lorsque le numéro de Rossby, basé sur la vitesse d'Ekman et l'échelle de longueur horizontale, approche des valeurs d'ordre un. Ces valeurs sont typiques, par exemple, dans le champ de stress glace-océan à travers des gradients prononcés tels que les pistes de la couverture de glace de mer. Des travaux récents ont montré une forte asymétrie dans les vitesses de pompage, le forçage cyclonique produisant des remontées d'eau diffuses et le forçage anticyclonique produisant des fronts de descente d'eau nets. Pour mieux comprendre cette dynamique, nous considérons la réponse stable à une simple prescription spécifiée du stress. Dans le plan (x - z) perpendiculaire au stress, la dynamique est décrite par l'équation de Navier-Stokes à deux dimensions, avec un terme de forçage dépendant du cisaillement vertical de la vitesse dans la direction y -hat, spécifié par une équation de quantité de mouvement sans pression. Une expansion dans un nombre de Rossby basé sur la vitesse d'Ekman est utilisée pour résoudre le système et pour mieux comprendre l'asymétrie. Les interactions avec la stratification et les courants géostrophiques sous-jacents sont également considérées, et des exemples de cas où ces effets pourraient être importants sont donnés. L'auto-advection du flux d'Ekman est importante dans ce phénomène asymétrique. Puisque l'asymétrie apparaît dans le champ de vorticité, l'auto-advection des termes d'Ekman joue un rôle plus important dans l'asymétrie upwelling-downwelling que le terme dissipatif. Les solutions sont stables avec l'ajout d'un bruit significatif, cependant des recherches supplémentaires sont nécessaires pour évaluer la source plus précise de l'asymétrie.

Acknowledgements

I would like to thank my supervisor David Straub for his guidance and endlessly insightful impromptu lectures that led to a deeper understanding of not just the ocean, but the research process as a whole. You showed me the tools to become fearless at exploring new topics and ideas, and I am forever grateful for this experience.

Thank you to Lizz, who made the harder days a whole lot brighter, and helping me every step of the way. Thank you to my parents for being my sources of stability in the midst of turbulence, and providing me with everything I would ever need in life to succeed. Thank you to my partner Ben, for constantly reminding me what I am capable of and always being my favourite person to talk to at the end of the day. You are all so incredibly important to me, and none of this would have been possible without you.

Lastly I want to thank my dear cat Charly, whose support was always in the form of much welcomed distractions and warm cuddles. Rest in peace little guy ♥

Table of Contents

Abstract	i
Abrégé	ii
Acknowledgements	iii
List of Figures	viii
List of Tables	ix
List of Symbols	x
1 INTRODUCTION	1
1.1 Formulation of Linear Ekman Theory	2
1.1.1 Equations of Motion	4
1.1.2 Ekman Pumping and Suction	6
1.2 Development of Nonlinear Ekman Theory	8
1.3 Beyond Classical Nonlinear Ekman Theory	9
1.3.1 Upwelling-Downwelling Asymmetry in the Arctic	9
2 NUMERICAL MODEL	13
2.1 Governing Equations	14
2.1.1 Full Derivation from Momentum Equations	15
2.1.2 Linear Case: Leading Order Solution	17
2.1.3 Nonlinear and Nth Order Approximations	18
2.2 Code Implementation	22
2.2.1 Nondimensionalization of Parameters	22

2.2.2	Testing Convergence of Solutions	25
2.2.3	Buoyancy	26
2.2.4	Time-Dependent Stability Analysis	27
3	RESULTS AND DISCUSSION	28
3.1	Near Convergence Steady Velocity Fields	28
3.1.1	Regime I: Small Ekman Rossby Number	28
3.1.2	Regime II: Moderate Ekman Rossby Number	29
3.1.3	Regime III: Large Ekman Rossby Number	30
3.2	Parameter Sensitivity	36
3.3	Time-dependent Solution and Stability Analysis	38
3.3.1	Stability analysis	39
3.4	Fourier Analysis	41
3.5	Conclusions	42

List of Figures

1.1	Figure obtained from [Vallis, 2006]. Idealized Ekman spiral forced by wind stress.	3
1.2	Vertical profile of a surface Ekman layer generated by wind stress, compared to the interior flow of the Ekman layer. Figure taken from [Cushman-Roisin and Beckers, 2011].	3
1.3	Figure obtained from [Vallis, 2006]. An idealized boundary layer where velocity field U varies rapidly near the boundary $z=0$ in order to satisfy the boundary conditions. This region is depicted as δ , which is the boundary layer thickness such $\delta \ll H$ where H is total distance away from boundary	4
1.4	Horizontal M_E and vertical mass transport W_E in the Ekman layer, resulting in 2D circulation cells. Positive W_E corresponds to Ekman pumping and negative corresponds to suction. Figure taken from [Vallis, 2006].	8
1.5	Upwelling-Downwelling asymetry. Figure taken from [Bourgault et al., 2020] . . .	11
1.6	Turbulent kinetic energy generation from mean kinetic energy (MKE) and potential energy (PE) in an intense downwelling and diffuse upwelling regime. Figure taken from [Bourgault et al., 2020].	11
1.7	Ice-ocean stress and salt flux profiles over a sea ice lead L_{lead} . Figure taken from [Bourgault et al., 2020]	12

2.1	Diagram showing how Nth order correction terms are computed. Superscripts denote the order number n ($0 \leq n \leq N$), except for on the gradient operator. At each order n , the set of equations give the solution to a state variable, say ψ^n , which is the n^{th} correction term such that the final n^{th} order approximation of ψ is $\Psi = \psi^0 + \psi^1 + \psi^2 + \dots + \psi^N$.	20
2.2	The maximum values for streamfunction strength as the order to which Ψ is corrected to (n) increases. This method is used for detecting convergence or divergence of solutions.	26
3.1	Colourmap depicts vertical velocity in the Ekman layer and contour lines represent streamfunction lines. Solutions computed for Regime I where $R_e = 0.2$	30
3.2	Colourmap depicts vertical velocity in the Ekman layer and contour lines represent streamfunction lines. Solutions computed for Regime II where $R_e = 0.9$	31
3.3	Colourmap depicts vertical velocity in the Ekman layer and contour lines represent streamfunction lines. Solutions computed for Regime III where $R_e = 1.75$	32
3.4	Plots for geostrophic forcing where $J(\psi, v_g)$ forces equation 2.32c. Colourmap depicts vertical velocity in the Ekman layer and contour lines represent streamfunction lines. Solutions computed for Regime III where $R_e = 1.75$.	34
3.5	Nonlinear component of terms is isolated by subtracting the linear approximation from the nth order approximation	35
3.6	Colourmap showing nonlinear contribution to vorticity (ζ minus the linear component (ζ^0)).	36
3.7	Ψ and ζ forced by different terms in horizontal momentum equation. Only NL contributions are plotted (order 0 solution subtracted). Contours correspond to streamfunction Ψ_A and Ψ_B	37
3.8	$R_E = 1.75$, $A_h = 1.08 \times 10^3 \text{ m}^2/\text{s}$, increased horizontal viscosity to exemplify the effect of higher Eddy viscosity while R_E remains the same as before.	38
3.9	Maximum ψ computed in regime with buoyancy flux, showing the divergence of solutions at higher orders of approximation.	39

3.10	Time dependent streamfunction solution at 11th, 71st, 131st and 541st iteration respectively. Simulation ran for a total of 6×10^4 seconds, or approximately 16.7 hours.	40
3.11	Large random background noise added to v at $t = 0$ in the form $1e - 3 * \text{noise}(zt - z)(z - zb)$ where <code>noise</code> is a Python-generated random seeded function.	41
3.12	Time dependent streamfunction with noise at 1st, 71st, 131st and 411st (final) iteration respectively.	42
3.13	The horizontal slice of Ψ^n from Regime III taken at the depth containing maximum streamfunction values, iterated over all orders of correction. This is the signal that we later take the Fourier transform of to analyze.	43
3.14	Power Spectrum of each 10th order taken of the signal shown in figure 3.13. Plotted on a logarithmic y- and x-axis to show the energy containing range, inertial subrange, and dissipation range.	44
3.15	The maximum values for streamfunction strength as the order to which Ψ is corrected to (n) increases. Shows that values above $R_E = 1.75$ do not converge. The oscillations in each run is noise from the model “trying” to converge.	45

List of Tables

3.1	Parameters used in all simulations	29
3.2	Parameters used in Regime I	29
3.3	Parameters used in Regime II	32
3.4	Parameters used in Regime III	33
3.5	Parameters used in Time-dependent Solution (no noise added)	39

List of Symbols

Notation	Description
b	Buoyancy
N	Brunt–Väisälä frequency or order of approximation
ρ	Density
f	Coriolis parameter
t	Time
x, y, z	Cartesian coordinates
\mathbf{u}	Two-dimensional Velocity (u,v)
\mathbf{v}	Three-dimensional Velocity (u,v,w)
w	Vertical velocity
\mathbf{F}	Friction/dissipative term or forcing term
\hat{k}	Wave vector with components (k,l,m)
$\hat{i}, \hat{j}, \hat{k}$	Unit vectors in (x,y,z) directions
L, H	Horizontal and vertical length scale
R_E, R_G	Ekman Rossby Number, Geostrophic Rossby Number
$\boldsymbol{\tau}$	Stress Vector
ψ	Streamfunction
ζ	Vertical Vorticity
p	Pressure
η	Kinematic viscosity
ϕ	Pressure divided by density

Notation	Description
A_h, A_v or A_x, A_z	Horizontal and Vertical Eddy-Viscosity coefficient

Chapter 1

INTRODUCTION

When looking at the surface of the ocean on a windy day, one notices at the very surface of the water that the movement follows the direction of the wind. If you were to stand at the shoreline on such a day then you would surely see the wind and waves in the same general direction at the surface, but if you were to stand in the ocean your feet won't feel as much of the effects of wind stress as your chest where the surface meets the air. This illustrates the intuitive dissipation of wind speed with depth through frictional forces between layers of water. What this does not capture, however, is the effect of a rotating Earth.

As the Earth rotates, so does our dynamical representation of fluids. In particular, the Coriolis force deflects the direction of water to the right of the wind stress in the Northern Hemisphere, and to the left in Southern Hemisphere. It follows that the flow of each subsequent layer of water is also deflected by Coriolis force and at a slower rate [Ekman, 1905]. This phenomenon is depicted in Figure 1.1 and referred to as the Ekman spiral, named after Vagn Wilfrid Ekman as he was the first to discover this dynamical phenomenon¹. From the surface of the water to the depth at which the effects of wind stress have dissipated, is called the Ekman layer. The vertical profile of the Ekman layer is shown in Figure 1.2. This layer is relatively thin ($O(10 - 10^2 \text{ m})$) compared to the entire depth of the ocean ($O(10^3 \text{ m})$), where the upper layer is primarily driven by wind stress and the lower layer driven by interaction of interior geostrophic velocity with a rigid lower surface.

¹This came decades before advances in oceanographic instrumentation in the 1980s which allowed for sufficiently sensitive measurements of velocity profiles at depth [Vallis, 2006]

In large scale oceanic flow where effects of rotation is large, the dominant balance in the momentum equation is between Coriolis and friction or stress terms in the boundary layer (i.e. the Ekman layer). More precisely, the balance is between Coriolis terms and the forces due to the stress generated small-scale turbulent motion and not molecular viscosity and diffusion in a direct sense – because then we would only consider scales on the order of centimeters. Since the stress comes from turbulence, this makes things more complex – it becomes nearly impossible to confidently determine its state with precision, so instead we look at general properties of the Ekman layer that are independent of knowing the precise form of the friction, and as it turns out we can learn a lot by doing just that [Vallis, 2006].

It is well understood that turbulence plays an important role in the dynamics of the Ekman layer and contribute to dynamical features observed, but its precise nature is unclear. The Ekman layer is of particular interest because of several reasons, one of it being the prevalence of turbulence and nonlinear motion, but also the fact that this is where atmosphere-ocean coupling models are important. Despite advanced instrumentation for oceanographic data, Ekman layer dynamics are more difficult to observe due to the rapid timescale and turbulence motion, leaving room to reconcile observations and theory via climate models.

1.1 Formulation of Linear Ekman Theory

We begin by introducing the main components of Ekman theory and its uses. The Ekman layer is the thin boundary layer near the surface of the ocean that where in large-scale circulation – effects of rotation are significant. Therefore the dominant balance is between Coriolis and frictional terms.

In order to analyze either atmospheric or oceanic Ekman layers some assumptions may be made. Let us recall that the atmospheric Ekman layer is near the ground while the oceanic Ekman layer is near the surface of the ocean and is therefore largely driven by wind. We may assume that the Ekman layer is Boussinesq, which is to say that variations in density ρ are very small. This assumption is a good one to make since the boundary layer in consideration is very thin. We may also assume that the Ekman layer has a finite depth which occurs in the interior of the ocean where

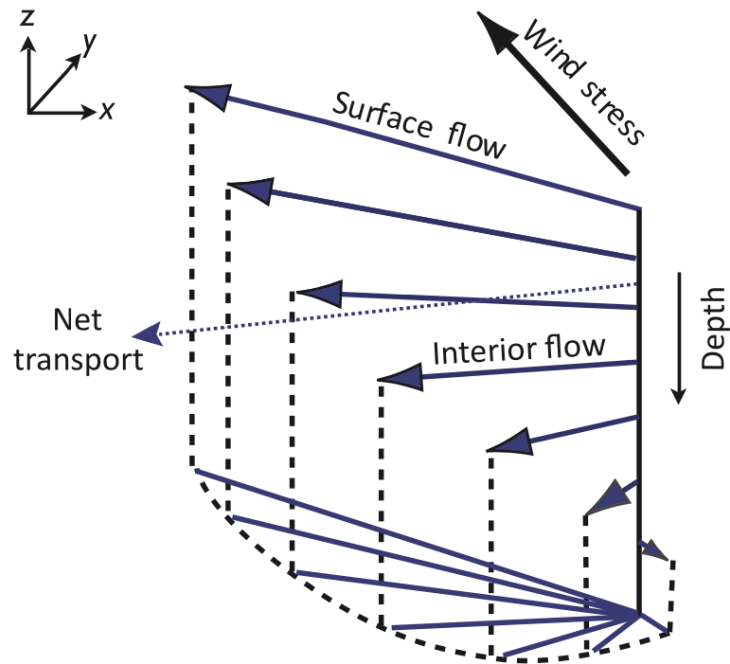


Figure 1.1: Figure obtained from [Vallis, 2006]. Idealized Ekman spiral forced by wind stress.

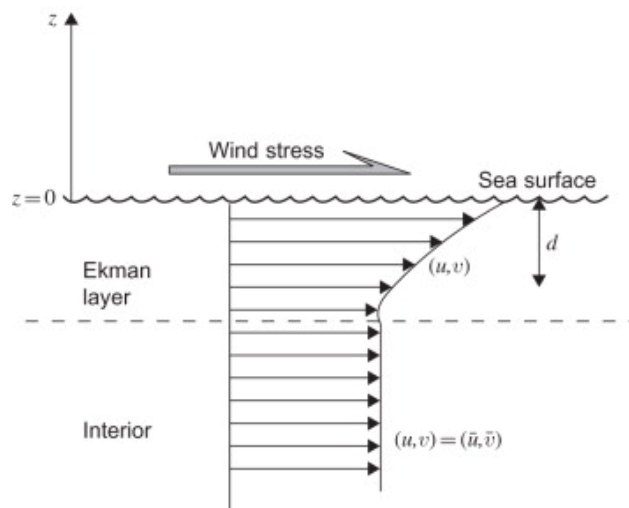


Figure 1.2: Vertical profile of a surface Ekman layer generated by wind stress, compared to the interior flow of the Ekman layer. Figure taken from [Cushman-Roisin and Beckers, 2011].

frictional stress nearly vanishes. It is also assumed that the nonlinear and time dependent terms in the equations of motion are ignored, while hydrostatic balance holds true vertically, and buoyancy is constant. Lastly we may parameterize friction by a viscous term of the form

$$\frac{\partial \tau}{\partial z} = A \frac{\partial^2 u}{\partial z^2},$$

where A is the eddy viscosity and τ is the stress, and τ/ρ_0 is the kinematic stress term.

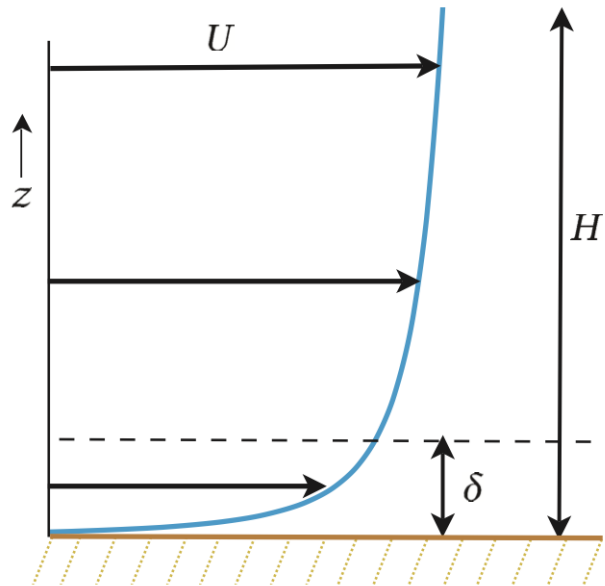


Figure 1.3: Figure obtained from [Vallis, 2006]. An idealized boundary layer where velocity field U varies rapidly near the boundary $z=0$ in order to satisfy the boundary conditions. This region is depicted as δ , which is the boundary layer thickness such $\delta \ll H$ where H is total distance away from boundary

1.1.1 Equations of Motion

Let us consider the fluid to be above a rigid surface ($z = 0$), and sufficiently far away from the boundary the velocity field is known and it is in geostrophic balance. Then the velocity field includes both a geostrophic and Ekman component:

$$\mathbf{u} = \mathbf{u}_g + \mathbf{u}_E . \quad (1.1)$$

To derive the Ekman equations we start with the horizontal momentum equation, where $\mathbf{u} = (u_e, v_e)$ is the Ekman velocity and $\frac{\partial}{\partial y} = 0$. The Frictional-geostrophic balance is as follows:

$$\mathbf{f} \times \mathbf{u} = \frac{1}{\rho_0} \frac{\partial \boldsymbol{\tau}}{\partial z} - \nabla \phi , \quad (1.2)$$

$$= A \frac{\partial^2 \mathbf{u}}{\partial z^2} - \nabla \phi , \quad (1.3)$$

where $\mathbf{f} = f \hat{k}$ and f is the Coriolis parameter, ϕ is pressure divided by density, and $\frac{\partial \boldsymbol{\tau}}{\partial z}$ represents the Reynolds-stress turbulence transmitting wind stress from the surface to ocean interior. The stress term can also be parameterized with eddy viscosity, where A is the coefficient of turbulent velocity.

The vertical momentum equation with constant buoyancy, b , gives

$$\frac{\partial \phi}{\partial z} = b = 0 . \quad (1.4)$$

Lastly it follows that Ekman equations must satisfy mass continuity. Thus our equation set becomes

$$\mathbf{f} \times \mathbf{u} = A \frac{\partial^2 \mathbf{u}}{\partial z^2} - \nabla \phi , \quad (1.5)$$

$$\frac{\partial \phi}{\partial z} = 0 , \quad (1.6)$$

$$\nabla \cdot \mathbf{v} = 0 . \quad (1.7)$$

The Ekman correction terms are negligible far away from the boundary layer. If only considering Ekman components then we can recall that there is no boundary layer in the pressure field,

thus equation 1.5 becomes:

$$\mathbf{f} \times \mathbf{u}_E = A \frac{\partial^2 \mathbf{u}}{\partial z^2}. \quad (1.8)$$

1.1.2 Ekman Pumping and Suction

Figure 1.3 depicts the vertical (W_E) and horizontal (M_E) ageostrophic mass transport in the Ekman layer. The upper Ekman layer is dominantly driven by wind stress while the bottom Ekman layer transport is driven by interactions with the interior geostrophic velocity and rigid surface at the bottom [Vallis, 2006]. From this it is evident that the Ekman pumping, W_E near the surface of the layer will differ if measured near the bottom. The expression for the top and bottom Ekman pumping (equations (1.12),(1.13)) can be deduced from frictional geostrophic balance and integrating over the layer thickness:

$$\mathbf{f} \times \mathbf{u}_E = \frac{1}{\rho_0} \frac{\partial \boldsymbol{\tau}}{\partial z}, \quad (1.9)$$

$$\mathbf{f} \times \mathbf{M}_E = \boldsymbol{\tau}_T - \boldsymbol{\tau}_B, \quad (1.10)$$

$$\text{where } \mathbf{M}_E = \int_{Ek} \rho_0 \mathbf{u}_E dz. \quad (1.11)$$

When calculating the bottom Ekman layer Mass transport, the stress at the top will be zero, and similarly for the top Ekman layer mass transport, the stress at the bottom will be zero. Using this and equation 1.10, we can write the mass transport as:

$$\text{top Ekman layer: } M_e = -\frac{1}{f} \mathbf{k} \times \boldsymbol{\tau}_T, \quad (1.12)$$

$$\text{bottom Ekman layer: } M_e = \frac{1}{f} \mathbf{k} \times \boldsymbol{\tau}_B. \quad (1.13)$$

The Ekman transport is always at right angles to the stress at the surface as we have previously discussed, and can now be seen by the cross product in equations 1.12, 1.13. This formulation is useful in the Ekman layer where the stress is primarily from wind, and since we only consider the top layer of the ocean it is generally independent of interior flow. In order to obtain vertical mass

transport, as is of interest in upwelling and downwelling, it can be obtained analytically beginning with integrating mass continuity equation over the Ekman layer:

$$\frac{1}{\rho_0} \nabla \cdot \mathbf{M}_{total} = -(w_T - w_B), \quad (1.14)$$

$$\mathbf{M}_{total} = \int_{Ek} \rho_0 \mathbf{u} dz, \quad (1.15)$$

$$= \int_{Ek} \rho_0 (\mathbf{u}_g + \mathbf{u}_E) dz, \quad (1.16)$$

$$\equiv \mathbf{M}_g + \mathbf{M}_E, \quad (1.17)$$

where the total mass transport is the sum of the geostrophic and ageostrophic component. As we did with the horizontal transport, we can set $W_T = 0$ in the top Ekman layer, and $W_B = 0$ in the bottom Ekman layer, where using 1.10 and the above equations gives:

$$\mathbf{k} \times (\mathbf{M}_{total} - \mathbf{M}_g) = \frac{1}{f} (\boldsymbol{\tau}_T - \boldsymbol{\tau}_B), \quad (1.18)$$

$$\implies \nabla \cdot (\mathbf{M}_{total} - \mathbf{M}_g) = \text{curl}_z [(\boldsymbol{\tau}_T - \boldsymbol{\tau}_B)/f], \quad (1.19)$$

where curl_z is the z-component of the curl. Plugging in equation 1.14 gives the bottom and top vertical velocities:

$$W_B = \frac{1}{\rho_0} \left(\text{curl}_z \frac{\boldsymbol{\tau}_T}{f} + \nabla \cdot \mathbf{M}_g \right), \quad (1.20)$$

$$W_T = \frac{1}{\rho_0} \left(\text{curl}_z \frac{\boldsymbol{\tau}_B}{f} - \nabla \cdot \mathbf{M}_g \right), \quad (1.21)$$

where we will omit the divergence of the geostrophic transport $\nabla \cdot \mathbf{M}_g$ since it is generally small compared to the other terms. Thus our vertical transport equations are as follows:

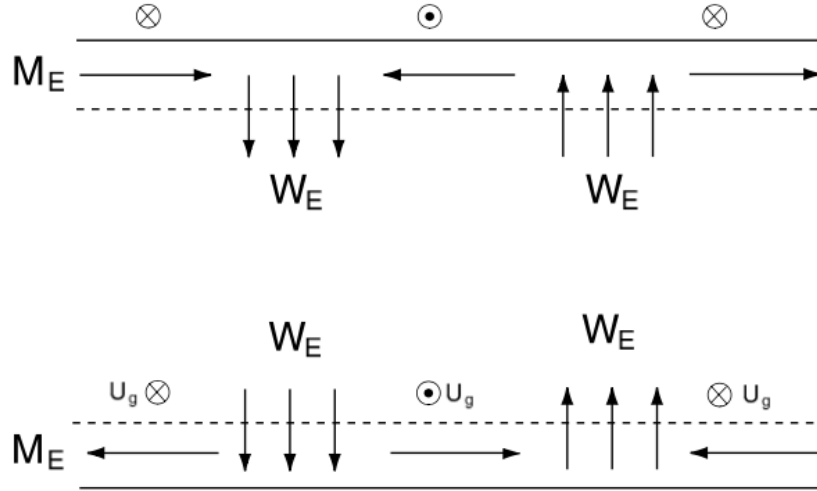


Figure 1.4: Horizontal M_E and vertical mass transport W_E in the Ekman layer, resulting in 2D circulation cells. Positive W_E corresponds to Ekman pumping and negative corresponds to suction. Figure taken from [Vallis, 2006].

$$W_B = \frac{1}{\rho_0} \left(\text{curl}_z \frac{\tau_T}{f} \right), \quad (1.22a)$$

$$W_T = \frac{1}{\rho_0} \left(\text{curl}_z \frac{\tau_B}{f} \right), \quad (1.22b)$$

demonstrating that the friction inducing a vertical velocity at the boundary of the Ekman layer is proportional to the curl of the stress at the surface – an incredibly powerful tool in Ekman theory. Its usefulness comes from the power to parameterize the layer using resolved/known values when numerical models often do not have the ability to explicitly solve an Ekman layer (usually due to a lack of vertical resolution and computational expense).

1.2 Development of Nonlinear Ekman Theory

The work of [Stern, 1965] and [Niiler, 1969] included tilting of vertical relative vorticity in Ekman theory, which is what is called nonlinear Ekman theory, whereby this inclusion modifies the Ekman pumping velocity such that a horizontally uniform wind stress can still drive vertical velocities (Stern 1965) [Wenegrat and Thomas, 2017]. A pertinent finding from [Wenegrat and Thomas,

2017] is that there is an improvement of accuracy of the calculated Ekman pumping velocity by retaining terms of higher order in the balanced Rossby number $R = U/fL$ by virtue of the Ekman pumping velocity itself being proportional to R . Thus including terms of $O(R^2)$ in the solution leads to an $O(R)$ relative improvement in accuracy [Wenegrat and Thomas, 2017].

It is interesting to note that although it is historically called “nonlinear” Ekman theory, these models rely on a known geostrophic velocity, which renders the system into one which can be linearized. Furthermore, all previous stipulations of nonlinear Ekman theory ignore the self-advecting Ekman flow, from now referred to as “Ekman-Ekman interactions”. These are found in the Ekman equations with terms such as $(\vec{u}_E \cdot \nabla)\vec{u}_E$, where $u_E = u - u_g$. This is typically neglected since the Ekman based Rossby number $R_E = \frac{U_E}{fL_E}$ is typically small, making the Ekman-Ekman interactions relatively negligible.

Hence the main focus of this thesis, which is to show how Ekman-Ekman interactions play a role in scenarios with higher Ekman-Rossby numbers.

1.3 Beyond Classical Nonlinear Ekman Theory

The presence of a high Rossby number $R = U/fL$ implies that $fL \ll U$ which could mean small f (like in low latitudes) or a length scale L that is very small. Thus, submesoscale (SM) flows are typically characterized by Rossby numbers of $O(1)$.

In Arctic sea ice leads, the forcing varies sharply across the width of a narrow lead as shown in Figure 1.7, meaning even weak friction layer currents can produce large Rossby numbers [Bourgault et al., 2020]. This sharp gradient in stress is responsible for increased small-scale horizontal activity which in turn leads to strong surface layer nonlinearity [Bourgault et al., 2020].

1.3.1 Upwelling-Downwelling Asymmetry in the Arctic

The work of Bourgault et al. considers the response to mechanical forcing across sea ice leads using large-eddy simulations. They considered a periodic domain similar to the one we will consider in Chapter 2, and took forcing to be given by a saw tooth profile (see Figure 1.5). This produced

an intense vorticity forcing over the lead balanced by a broad vorticity forcing on the opposite sign elsewhere. Their results show strong asymmetry between anticyclonic and cyclonic forcing, with a focused downwelling associated with strong turbulence, and diffuse upwelling with weak turbulence [Bourgault et al., 2020]. This asymmetry contributes to the additional heat flux and turbulence heat fluxes underneath the lead. The turbulent kinetic energy beneath the ice lead in Figure 1.6 shows that the shear production (downwelling) provides a clear source of turbulent kinetic energy and buoyancy production (upwelling) provides a weak sink. This points to a key result from their work which was that an anticyclonic forcing over the lead led to a large input of turbulent kinetic energy there (Figure 1.6).

Linear Ekman theory suggests that the Ekman pumping is proportional to the curl of the stress. This proportionality is not seen in upwelling-downwelling asymmetry (UDA) which makes this a phenomenon worth investigating further. The dynamical origins of UDA has been examined by others but they find that the the asymmetries are due to interactions of Ekman pumping with underlying currents [Stern, 1965], [Hart, 1995], [Wenegrat and Thomas, 2017]. The work of [Duquette et al., 2019] found the asymmetry to be not to be related to nonlinear interactions with the underlying currents, but rather to nonlinear interactions in which the surface Ekman-like flow advects. This is found to be significant when Rossby numbers approach $R = \frac{U}{fL} \sim O(1)$ values, which can either happen for very small f (for instance near the equator) or for motion across small length scales. This is why we are able to achieve high Rossby numbers across sharp gradients in forcing such as narrow sea ice leads. In Bourgault et al.'s simulations, the Rossby number in upwelling was about 9 and in downwelling case was 80 [Bourgault et al., 2020], corresponding to the circulation cells in Figure 1.5.

We seek to further our understanding of the dynamical origins of UDA based on findings from [Bourgault et al., 2020] and [Duquette et al., 2019]. This thesis investigates this phenomenon by approaching the problem from the bottom up, by modelling the UDA through dynamic equations of the Ekman layer as opposed to using a global climate model.

The role of submesoscale dynamics of mid-latitude regions in upper-ocean dynamics is well understood in oceanographic literature, while much less is understood about submesoscale dynam-

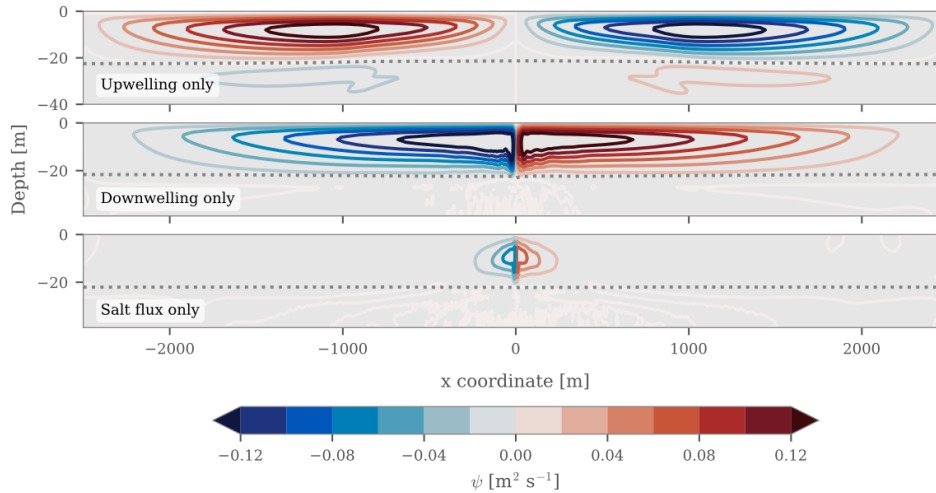


Figure 1.5: Upwelling-Downwelling asymmetry. Figure taken from [Bourgault et al., 2020]

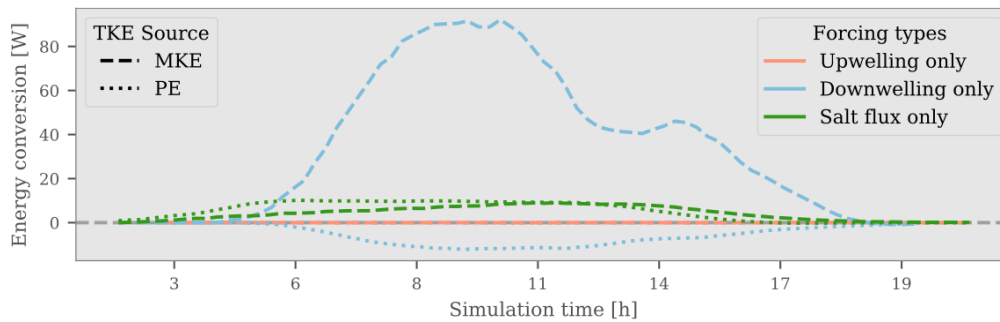


Figure 1.6: Turbulent kinetic energy generation from mean kinetic energy (MKE) and potential energy (PE) in an intense downwelling and diffuse upwelling regime. Figure taken from [Bourgault et al., 2020].

ics in the Arctic [Mensa and Timmermans, 2017]. This could be particularly important since it has been suggested that lateral SM flows under sea ice is greatly underestimated in general circulation models [Stroeve et al., 2007]. More pertinent to our research, we know that small-scale flows are often associated with vertical velocities which can enhance ocean-to-ice heat fluxes – naturally, these flows may have serious consequences to sea-ice cover [Mensa and Timmermans, 2017]. Any improvement to models involving these small-scale flows could have the potential to improve the accuracy and prediction of sea-ice cover melt.

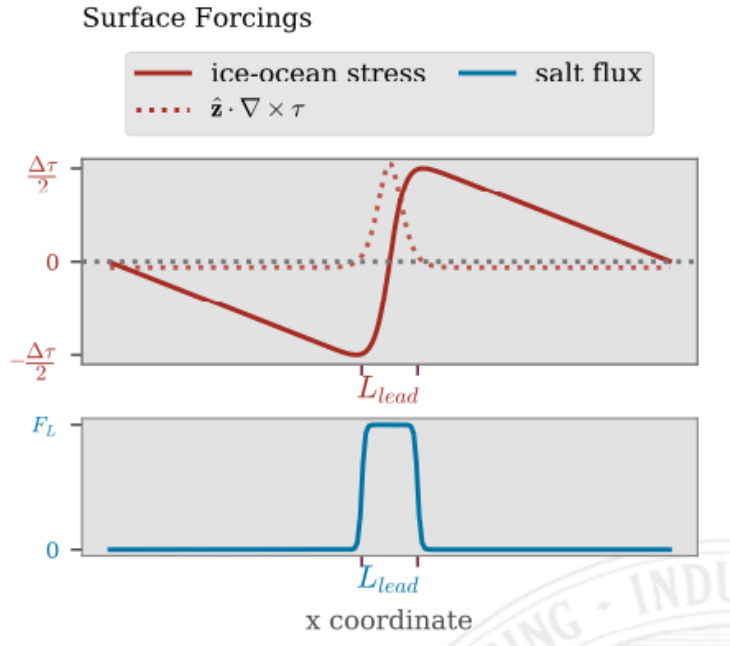


Figure 1.7: Ice-ocean stress and salt flux profiles over a sea ice lead L_{lead} . Figure taken from [Bourgault et al., 2020]

As discussed, this thesis investigates the dynamical origins of UDA. One possible origin is the transients in Reynold’s stress term, where the transients feed back onto the mean state. This however is out of the scope of the thesis, where we will only be considering a steady-state version of the problem. As such, the focus will be to investigate whether nonlinearity related to the mean advection itself. The central ideal is to solve a steady nonlinear Ekman problem using a perturbation method and look for any potential asymmetry, and if so to attempt to understand it better.

Chapter 2

NUMERICAL MODEL

The purpose of the model is to explicitly solve for the steady-state boundary value Ekman layer problem in the x - z plane. To do so, we use a framework which allows for solving differential equations using spectral methods, and utilizes Message Passing Interface (MPI) parallelization. Thus the program was written in python 3.2 in conjunction with an open-source python framework called Dedalus [Burns et al., 2020].

We aim to primarily investigate the importance of Ekman-Ekman nonlinearity – by which we mean Ekman terms multiplied by one another (see equation 2.31)– in a steady upwelling-downwelling asymmetry regime. We do so by assuming a z -independent geostrophic flow in order to explicitly solve the x - z nonlinear Ekman layer problem.

An expansion is implemented where the assumed Ekman solution for velocity v is used to compute streamfunction Ψ , where Ψ is implied from v_z and vice versa, therefore a new correction is computed at each step. What we hope to find is that in this regime the corrections display stronger upwelling-downwelling asymmetry as the order increases. Our a priori expectation is that this is due to the slow part of the flow advecting the y -vorticity anomalies in the x -direction interacting with the quadratic interactions of near-inertial waves which feedback onto the slow part.

To start, we will make a 2D model of the Ekman layer, periodic (Fourier basis) in x and Chebyshev in z . A constant wind stress is applied to the surface layer causing larger momentum flux near the surface and minimal to none near the bottom surface (fixed, for the purposes of the simulation).

2.1 Governing Equations

In the following sections, a subscript of either x, y, or z denotes a partial derivative taken in the respective direction.

We seek a solutions for streamfunction ψ using Ekman equations. Assessing the problem in the x-z plane, with a constant density fluid in the x-z plane but allowing for $v \neq 0$, we state the pressureless Navier-Stokes equation, taking vertical shear in the y-direction as forcing. The full equations include time dependence are as follows:

$$\vec{u}_t + \vec{u} \cdot \nabla \vec{u} + f \hat{z} \times \vec{u} = -\nabla \phi - A \nabla^2 \vec{u}, \quad (2.1)$$

$$\nabla \cdot \vec{u} = 0, \quad (2.2)$$

$$\partial_y \longrightarrow 0. \quad (2.3)$$

We now have a set of equations reminiscent of the Ekman equations plus a total derivative of velocity term on the LHS of our Navier-Stokes simplification. Expanding the vector form into component form, we get:

$$u_t + \underbrace{uu_x + wu_z}_{\text{Non-linear}} - fv = -\phi_x + A(u_{xx} + u_{zz}), \quad (2.4)$$

$$v_t + \underbrace{uv_x + wv_z}_{\text{Non-linear}} + fu = A(v_{xx} + v_{zz}), \quad (2.5)$$

$$w_t + \underbrace{uw_x + ww_z}_{\text{Non-linear}} = -\phi_z + A(w_{xx} + w_{zz}). \quad (2.6)$$

Removing time-dependence we get our steady problem governing equations:

$$uu_x + wu_z - fv = -\phi_x + A(u_{xx} + u_{zz}), \quad (2.7a)$$

$$uv_x + wv_z + fv = A(v_{xx} + v_{zz}), \quad (2.7b)$$

$$uw_x + ww_z = -\phi_z + A(w_{xx} + w_{zz}). \quad (2.7c)$$

Note that in the above equations, the dissipation terms are written assuming an isotropic viscous coefficient A . In our simulations we ultimately replace this with anisotropic coefficients such that $A\nabla^2 = A_h\partial_x^2 + A_v\partial_z^2$. For notational simplicity this will often be written below in isotropic form however.

2.1.1 Full Derivation from Momentum Equations

Using the relationship between streamfunction ψ , velocity (u, v, w) and relative vorticity ζ

$$\zeta = \nabla^2\psi = u_z - w_x \quad (2.8)$$

$$u = \psi_z \quad (2.9)$$

$$w = -\psi_x \quad (2.10)$$

We take the x-z momentum equations 2.4 and 2.6, and take the \hat{y} component of the curl of the equations :

$$\frac{\partial(2.4)}{\partial z} \implies u_z u_x + u u_{xz} + w_z u_z + w u_{zz} - f v_z = -\phi_{xz} + A(u_{xxz} + u_{zzz}) \quad (2.11)$$

$$\frac{\partial(2.6)}{\partial x} \implies u_x w_x + u w_{xx} + w_x w_z + w w_{zx} = -\phi_{zx} + A(w_{xxx} + w_{zzx}) \quad (2.12)$$

$$\frac{\partial(2.4)}{\partial z} - \frac{\partial(2.6)}{\partial x} \implies u_z u_{xz} + w_z u_{zz} - u_x w_{xx} - w_x w_{zx} - f v_z = A((u_{xxz} + u_{zzz}) - (w_{xxx} + w_{zzx})) \quad (2.13)$$

$$\implies w_z(u_z - w_x) + u_x(u_z - w_x) + J(\psi, \zeta) = A\nabla^2(u_z - w_x) \quad (2.14)$$

$$\implies \zeta \overbrace{(u_x + w_z)}^0 + J(\psi, \zeta) = f v_z + \nabla^2 \zeta \quad (2.15)$$

$$\implies \boxed{J(\psi, \zeta) = f v_z + A\nabla^2 \zeta} \quad (2.16)$$

where $J(A, B) = A_z B_x - A_x B_z$ is the Jacobian operation of variables A, B . Simplifying the v -momentum equation 2.5 by using streamfunction notation, we get our second state equation:

$$uv_x + wv_z = -fu + A\nabla^2 v \quad (2.17)$$

$$\psi_z v_z - \psi_x v_x = -fu + A\nabla^2 v \quad (2.18)$$

$$\boxed{J(\psi, v) = -fu + A\nabla^2 v} \quad (2.19)$$

Therefore equations 2.16 and 2.19 are the governing equations for the model, derived from our original momentum equation.

Boundary Conditions

The variables we've stated explicitly for our solver to take in are $\psi, u, v, v_z, w, \zeta, \zeta_z$ (7 variables).

The boundary conditions should be such that there is no stress in the u -direction from top or bottom (free-slip condition), similarly for v -direction but with top being $\sin x$ stress and $v_z = 0$ at the bottom. The free slip boundary conditions make the bottom Ekman layer minimal since that is not our focus in this study. This causes an issue however where the y -momentum budget cannot be easily balanced. To rectify this we add a linear damping term (with coefficient r) on the geostrophic velocity. Since our geostrophy is z -independent as prescribed by the model, we can substitute $v_g = \int_0^H v dz = \bar{v}$.

$$\psi|_{\text{top}} = 0 \quad (2.20)$$

$$\psi|_{\text{bottom}} = 0 \quad (2.21)$$

$$v_z|_{\text{top}} = \frac{\tau_0}{A} \sin(xk + \frac{\pi}{2}) \quad (2.22)$$

$$v_z|_{\text{bottom}} = 0 \quad (2.23)$$

$$u_z|_{\text{top}} = 0 \quad (2.24)$$

$$u_z|_{\text{bottom}} = 0 \quad (2.25)$$

$$(2.26)$$

where $k = \frac{2\pi}{L}$ and τ_0 is the wind forcing. For orders above 0 (i.e. all nonlinear adjustments), the wind forcing is $\tau_0 = 0$ since the adjustments themselves need no additional forcing to the base case.

2.1.2 Linear Case: Leading Order Solution

The leading order solution to the problem is the linear solution, therefore the nonlinear terms in our momentum equations 2.4-2.6 are set to zero. Equivalently, we can set the LHS of equations 2.32a and 2.32c to zero, shown below:

$$A\nabla^2 v - fu = 0 \quad (2.27)$$

$$A\nabla^4 \psi + fv_z = 0 \quad (2.28)$$

In order to ensure the problem remains top trapped and free slip at the bottom of our domain, a damping term $r\bar{v} = r\left(\frac{1}{H}\right)\int_0^H v dz$ is added, where r is a factor that is sufficiently small for convergent solutions, and \bar{v} is the vertically averaged velocity in the y-direction.

$$\begin{aligned} A\nabla^2 v - r\bar{v} - fu &= 0 \\ A\nabla^2 \zeta + fv_z &= 0 \end{aligned}$$

2.1.3 Nonlinear and Nth Order Approximations

For the derivation of the nonlinear equations, we keep the nonlinear terms in the momentum equations and thus keep the Jacobian terms in equations 2.32a and 2.32c. ¹

$$A\nabla^2 v - r\bar{v} - fu = J(\psi, \zeta) \quad (2.32a)$$

$$A\nabla^2 \zeta + fv_z = \vec{u} \cdot \nabla v \quad (2.32b)$$

$$= J(\psi, v) \quad (2.32c)$$

The nonlinear terms (the Jacobians) are approximated using the linear solution, the linear solution being the **zeroth-order approximation**. In the linear case, the forcing has a $\sin(kx)$ structure and a $\sin(kx)$ response. As the order of approximation increases, so does the wavenumber k . Let us denote the order of the solution as superscript (unless on gradient), where \mathbf{u}^0 is the leading order solution and $\mathbf{F}^0 = -(\mathbf{u}^0 \cdot \nabla)\mathbf{u}^0$ is the forcing (with a $\sin(2kx)$ structure and $\sin(2kx)$ response) used to obtain \mathbf{u}^1 solutions, as presented in the equations below:

$$f\hat{z} \times \mathbf{u}^1 = \mathbf{F}^0 - \nabla\phi^1 + \nu\nabla^2\mathbf{u}^1 \quad (2.33)$$

$$\nabla \cdot \mathbf{u}^1 = 0 \quad (2.34)$$

¹Note that if we expand the RHS equation 2.32b (ignoring the viscosity factor) into the geostrophic and Ekman components, we obtain a clear indication of where the Ekman-Ekman terms occur:

$$\vec{u} \cdot \nabla v = (\vec{u}_g + \vec{u}_E) \cdot \nabla(v_g + v_E) \quad (2.29)$$

$$= (u_g + u_E, w_g + w_E)(v_{gx} + v_{Ex}, v_{gz} + v_{Ez}) \quad (2.30)$$

$$= u_g v_{gx} + u_g v_{Ex} + u_E v_{gx} + u_E v_{Ex} + w_g v_{gz} + w_g v_{Ez} + w_E v_{gz} + w_E v_{Ez} \quad (2.31)$$

In order to compute order 2 solutions, the forcing now becomes $\mathbf{F}^1 = -(\mathbf{u}^0 \cdot \nabla)\mathbf{u}^1 - (\mathbf{u}^1 \cdot \nabla)\mathbf{u}^0$. This forcing \mathbf{F}^1 has a structure made of $\sin(kx)$ and $\sin(3kx)$ components, since the \mathbf{u}^1 has $\sin(2kx)$ structure (with frequencies near $\omega = 0, f, 2f$). Note that the structure of \mathbf{u}^n always corresponds to that of \mathbf{F}^{n-1} .

$$f\hat{\mathbf{z}} \times \mathbf{u}^2 = \mathbf{F}^1 - \nabla\phi^2 + \nu\nabla^2\mathbf{u}^2 \quad (2.35)$$

$$\nabla \cdot \mathbf{u}^2 = 0 \quad (2.36)$$

$$(2.37)$$

In order to compute higher order (Nth order) nonlinear approximations, we take the sum of all corrections until the Nth order correction computed. This process is shown in the diagram in Figure 2.1. As we can see in this flow chart, in order to solve the $n = 2$ order correction we need to compute a sum of Jacobians. These Jacobians correspond to the forcing \mathbf{F}^n denoted above.

Jacobian Operator in higher order computations

It is clear in the linear case that the expansion of $\vec{u} \cdot \nabla v$ with streamfunction notation can be written as a Jacobian (see equations 2.32a and 2.32c). In higher order approximations however, these advective terms become more complex. Since the Jacobian is the nonlinear component of our equations, it's important to create a regime that allows for Ekman self-advection. Suppose the 0th order solutions have been found, i.e. solutions to equations 2.27, 2.28. To compute the 1st order approximation, we need to solve our equations in $\mathcal{O}(1)$ by forcing the LHS with the Jacobian of the linear solution, i.e. $\mathbf{J}^0 = \mathbf{F}^0 = f\nu_z^1 + A\nabla^2\zeta^1$ needed as a forcing to compute solutions of order 1. To compute $\mathcal{O}(2)$, the forcing now becomes the sum of Jacobians corresponding to the sum of advective terms.²

²The sum of advective terms is to ensure that we have all interactions between different ordered solutions, i.e. self advection. It also is described in such a way that avoids double counting terms once Jacobians are expanded.

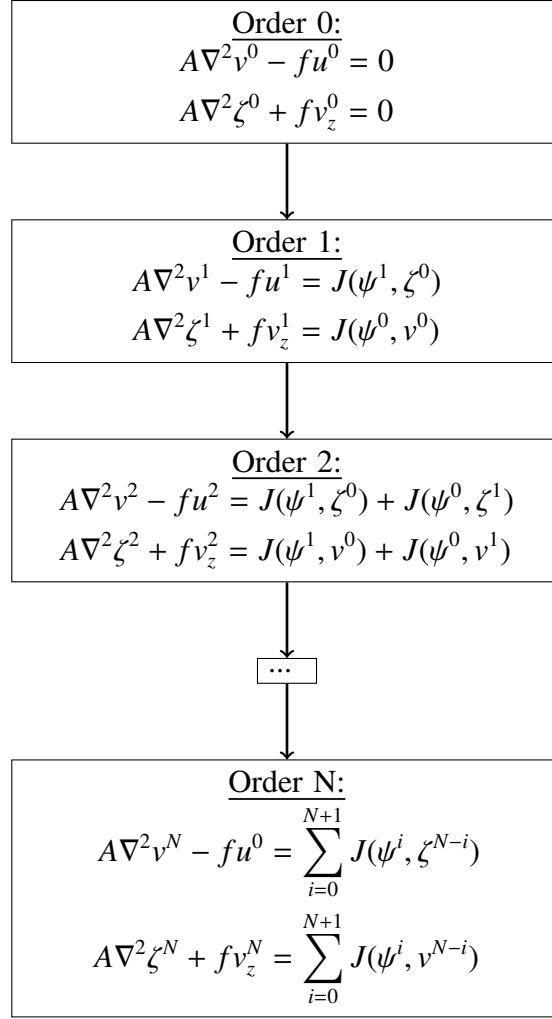


Figure 2.1: Diagram showing how Nth order correction terms are computed. Superscripts denote the order number n ($0 \leq n \leq N$), except for on the gradient operator. At each order n , the set of equations give the solution to a state variable, say ψ^n , which is the n^{th} correction term such that the final n^{th} order approximation of ψ is $\Psi = \psi^0 + \psi^1 + \psi^2 + \dots + \psi^N$.

$$0 = fv_z^0 + A\nabla^2\zeta^0 \quad (2.38)$$

$$\mathbf{J}^0 = fv_z^1 + A\nabla^2\zeta^1 \quad (2.39)$$

$$\mathbf{J}^1 = fv_z^2 + A\nabla^2\zeta^2 \quad (2.40)$$

$$= \mathbf{J}(\psi^1, \zeta^0) + \mathbf{J}(\psi^0, \zeta^1) \quad (2.41)$$

$$\mathbf{J}^2 = fv_z^3 + A\nabla^2\zeta^3 \quad (2.42)$$

$$= \mathbf{J}(\psi^0, \zeta^2) + \mathbf{J}(\psi^2, \zeta^0) + \mathbf{J}(\psi^1, \zeta^1) \quad (2.43)$$

Below is a matrix of all permutations of the orders of ψ and ζ respectively which appear as we expand $\mathbf{J}(\psi^N, \zeta^N)$, and we find that only the diagonal entries contain the permutations that would appear as we solve to order $N = 2$. For instance the matrix entry for all permutations of \mathbf{J}^2 would be $\{(0, 2), (1, 2), (2, 2), (0, 1), (1, 0), (1, 2), (0, 0), (2, 0), (2, 1)\}$ where the pair of numbers corresponds to the order of (ψ, ζ) which the Jacobian takes in the expansion of $J(\psi^2, \zeta^2) = J(\psi^0, \zeta^2) + (\psi^1, \zeta^2) + \dots + (\psi^2, \zeta^1)$. Recall that the Jacobian expansion ought to represent order n advective terms, and this expansion of $J(\psi^N, \zeta^N)$ illustrates that this will not correspond to the advective term at order n , and only a few of them will actually appear. This is how the general \mathbf{J}^N fixes this – by only selecting the permutations that correspond to the advective term expansion. The same principle and process applies to determining $\mathbf{J}(\psi^N, v^N)$:

$$\begin{bmatrix} 0,0 & 1,0 & 2,0 \\ 0,1 & 1,1 & 2,1 \\ 0,2 & 1,2 & 2,2 \end{bmatrix} .$$

This is then continued to the Nth order, the Jacobians calculated at each order can be expressed as the following sum:

$$\begin{aligned} \mathbf{J}^N(\psi, \zeta) &:= \sum_{i=0}^N \mathbf{J}(\psi^i, \zeta^{N-i}) \\ \mathbf{J}^N(\psi, v) &:= \sum_{i=0}^N \mathbf{J}(\psi^i, v^{N-i}) \end{aligned} \tag{2.44}$$

These appear as forcing terms at each order on the RHS of the equations to solve for the $n - 1$ order correction term in Figure 2.1.

2.2 Code Implementation

This numerical model was programmed in python using Dedalus [Burns et al., 2020], which is an open-sourced MPI-parallelized python framework for solving differential equations using spectral methods. This is particularly useful in this model since the problem can easily be represented in a spectral domain, where the x-axis is Fourier representable and z-axis is chebyshev. The choice of z-axis to use chebyshev basis is based on the fact that we require the highest resolution near the boundaries – in particular the top boundary. We need more resolution at the surface of the ocean where the main physical forcing is. The chebyshev basis provides just that, by containing grid points which are unevenly spaced, where they are more spaced out near the center of the domain and closer together near the boundaries.

2.2.1 Nondimensionalization of Parameters

In order to ensure the relative order of magnitude of the parameters chosen reflect a realistic Ekman layer, while adhering to our constraints, we nondimensionalize the parameters using Buckingham Pi theorem. We have length and time scale as dimensions, and height, length scale, viscosity, Coriolis parameter, damping parameter and wind forcing amplitude as variable parameters. Since we want to use the model to investigate the flow's behaviour at different Ekman-Rossby (R_e) and Geostrophic-Rossby (R_g) numbers, we would like to write them as a function of our parameters

such that the model can compute the parameters given a particular Rossby number. Similarly, the aspect ratio, Δa , of vertical to horizontal scales, and height ratio, Δh , of Ekman layer thickness to total depth of layer, must be written as functions in terms of the parameters. This is in order to be able to freely specify to the model both of these values to ensure that the regime has a sufficiently large horizontal length scale compared to vertical scale (as required for thin-boundary layer approximations) and that the Ekman layer remains significantly top trapped compared to the entire vertical length scale of the domain.

Dimensions: L, T

Parameters: H, L, A, f, r, τ_0

$$\Delta h = h_e/H \quad (2.45)$$

$$\Delta a = H/L \quad (2.46)$$

$$R_e = \frac{\tau_0}{f^2 L h_e} \quad (2.47)$$

$$R_g = \frac{\tau_0}{r H f L} \quad (2.48)$$

where $h_e = \sqrt{2A/f}$ is the Ekman layer thickness, a is the aspect ratio, and τ_0 includes the division by density ρ for simplicity (i.e. assumes $\rho = 1$).

Now we can fix f and H so that all dimensional quantities can be written in terms of f , H and functions of nondimensional parameters:

$$A = fH^2 \left(\frac{\Delta h^2}{2} \right), \quad (2.49)$$

$$L = \frac{H}{\Delta a}, \quad (2.50)$$

$$\tau_0 = f^2 H^2 R_e \left(\frac{\Delta h}{\Delta a} \right), \quad (2.51)$$

$$r = f \Delta h \left(\frac{R_e}{R_g} \right). \quad (2.52)$$

The viscous coefficient is set as follows:

$$\Delta h = h_e / H, \quad (2.53)$$

$$= \frac{\sqrt{2} A^{1/2}}{f^{1/2} H}, \quad (2.54)$$

$$\implies A^{1/2} = \frac{\Delta h f^{1/2} H}{\sqrt{2}}, \quad (2.55)$$

$$\implies A = \Delta h^2 f H^2 / 2. \quad (2.56)$$

We let this now be equal to the vertical viscosity A_v , such that the horizontal viscosity A_h is greater by some factor. The horizontal viscosity relation is found as follows:

The horizontal viscosity tends to be more sensitive to the resolution of the model, and needs to be high enough such that the solutions do not blow up or acquire excessive model noise. As such, the goal is to be able to resolve for the area of the contour plot where the data is closest together – this would be the downwelling jet. This distance will be equal to $U\lambda$ where $U = \tau/h_e$ and $\lambda = n_\lambda \Delta x$ is the wavelength in terms of the number of desired grid points in the jet, n_λ , and the size of each grid cell, $\Delta x = L/n_x$. Note that the value of n_λ is the one we will later be varying in order to increase or decrease A_h later in Chapter 3. Therefore the horizontal viscosity is

$$\implies A_h = U\lambda \quad (2.57)$$

$$= \left(\frac{\tau}{h_e} \right) n_\lambda \left(\frac{L}{n_x} \right) \quad (2.58)$$

$$\frac{\tau_0}{R_e} = h_e f^2 L, \quad (2.59)$$

$$= \frac{\sqrt{2}A^{1/2}}{f^{1/2}} f^2 L = \sqrt{2} f^{3/2} A^{1/2} L, \quad (2.60)$$

$$= \sqrt{2} f^{3/2} L (\Delta h^2 f H^2 / 2)^{1/2} \quad (\text{by equation 2.56}), \quad (2.61)$$

$$= \Delta h f^2 H L = \Delta h H \left(\frac{H}{\Delta a} \right) f^2, \quad (2.62)$$

$$\Rightarrow \tau_0 = \frac{\Delta h}{\Delta a} H^2 f^2 R_e, \quad (2.63)$$

$$r = \frac{\tau_0}{R_g H f L}, \quad (2.64)$$

$$= \frac{\Delta h}{\Delta a} H^2 f^2 R_e \frac{1}{H f L}, \quad (2.65)$$

$$\Rightarrow r = \Delta h \frac{R_e}{R_g} f. \quad (2.66)$$

The full steady-state equations with nondimensional parameters are:

$$\alpha \left(\frac{k_n^2}{h_e^2} \right) \left(\frac{\Delta h^2 f H^2}{2} \right) v_{xx} + \left(\frac{\Delta h^2 f H^2}{2} \right) v_{zz} - \left(f \Delta h \left(\frac{R_e}{R_g} \right) \right) \bar{v} - f u = J(\psi, v), \quad (2.67)$$

$$\alpha \left(\frac{k_n^2}{h_e^2} \right) \left(\frac{\Delta h^2 f H^2}{2} \right) \zeta_{xx} + \left(\frac{\Delta h^2 f H^2}{2} \right) \zeta_{zz} - f v_z = J(\psi, \zeta), \quad (2.68)$$

$$v_z(z=\text{top}) = \left(\frac{\Delta h H^2 f^2 R_e}{\Delta h^2 f H^2 / 2} \right) \cos(kx + \frac{\pi}{2}). \quad (2.69)$$

2.2.2 Testing Convergence of Solutions

The amplitude of the correction term should in theory exponentially decrease as order increases. Thus, the final solution should be when the maximum value of the correction term approaches zero, or very close to compared to the 0th order max value. Therefore when higher orders do not converge to zero, and in fact exponentially increase, we can conclude that these solutions are divergent, and thus are not robust. It must be noted that the model needs to be computed to high

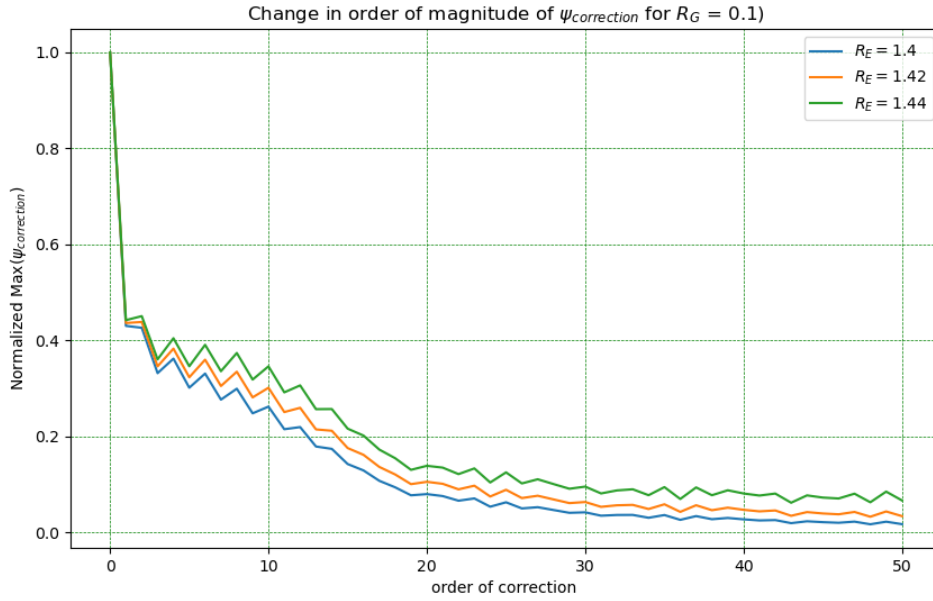


Figure 2.2: The maximum values for streamfunction strength as the order to which Ψ is corrected to (n) increases. This method is used for detecting convergence or divergence of solutions.

enough orders that the solutions do not just appear to be convergent with hidden divergence in orders above the one computed to. This can be a constraint in model, however this is why we choose to define convergence when each order's maximum solution value is consistently (across 10+ orders) monotonically decreasing. Figure 2.2 shows the the comparison of the maximum value of ψ found at each order correction for three different Ekman Rossby numbers, all of which converge.

2.2.3 Buoyancy

The standard equations we have derived thus far assume constant buoyancy, however in Chapter 3 we examine how the convergence of solutions and dynamical properties change with the inclusion of buoyancy flux at high Ekman-Rossby values.

To do so, the equations are amended to include buoyancy flux ³:

$$A\nabla^2 v - r\bar{v} - fu = 0, \quad (2.70)$$

$$A\nabla^2 \zeta + fv_z - b_x = 0, \quad (2.71)$$

$$A\nabla^2 b + wN^2 = 0, \quad (2.72)$$

$$\iint b \, dx dz = 0, \quad (2.73)$$

where N is the Brunt–Väisälä frequency, and its square equals the background vertical buoyancy flux, $N^2 = \overline{b_z}$. It follows that $0 < N^2 \ll f^2$, thus a conservative choice of frequency would be $N = 0.1f$.

2.2.4 Time-Dependent Stability Analysis

$$v_t - (A_h v_{xx} + A_v v_{zz}) + r\bar{v} + fu = -(\psi_x v_z - \psi_z v_x) \quad (2.74)$$

$$\zeta_t - (A_h \zeta_{xx} + A_v \zeta_{zz}) + fv_z = -(\psi_x \zeta_z - \psi_z \zeta_x) \quad (2.75)$$

The timestepping scheme used to solve this set of equations is the 1st-order semi-implicit BDF (backward Euler) scheme based on equation 2.6 from [Wang and Ruuth, 2008]. This scheme is implemented by Dedalus as part of their ODE integrator classes for timestepping [Burns et al., 2020].

³note that vertical velocity w is implemented in the code by substituting for its equivalent form, $-\psi_x$

Chapter 3

RESULTS AND DISCUSSION

To effectively diagnose the driving factors in upwelling-downwelling asymmetry we compute the solutions to an n th order approximation as described in Chapter 2, while increasing R_e and keeping R_g constant. In the next section we consider three regimes, where $R_e \ll 1$, $R_e < 1$, and $R_e > 1$. A summary of the parameters and values used in all regimes is shown in table 3.1.

Furthermore, a time-dependent version of the equations is simulated in order to test the stability of the upwelling-downwelling asymmetry under a forcing of additional noise. Results from the time-dependent solution are then compared to the steady case in terms of their parameter sensitivity, convergence limits, and general dynamics.

3.1 Near Convergence Steady Velocity Fields

In this section we will examine three Regimes where the Ekman Rossby number approaches $O(1)$ as previously mentioned. We will look at the first few order approximations ($n=0,1,2$) and then see the convergent solution.

3.1.1 Regime I: Small Ekman Rossby Number

In this regime, the Ekman Rossby number value is $R_e \ll 1$, specific values found in table 3.2. For such small Rossby number values we would not expect difference between the linear state and

Parameter	meaning	value
nx	number of x-grid points	512
nz	number of z-grid points	68
L	Length of domain (m)	20000m
H	Height/Depth of domain (m)	200m
h_e	Ekman layer thickness (m)	20m

Table 3.1: Parameters used in all simulations

Parameter	meaning	value
R_e	Ekman Rossby Number	0.2
R_g	Geostrophic Rossby Number	0.1
A_h	Horizontal viscosity	$6.22 \times 10^1 \text{ m}^2/\text{s}$
A_v	Vertical viscosity	$2 \times 10^{-2} \text{ m}^2/\text{s}$
r	Damping parameter parameter	2×10^{-5}
f	Coriolis parameter	10^{-4} rads/s
τ_0	Wind Forcing Amplitude	1.27×10^{-4}
N	Max order of approximation	6

Table 3.2: Parameters used in Regime I

computing higher order approximations, since the Ekman-nonlinearity in this regime would be very small. As is expected, Fig. 3.1 shows that the convergent state has symmetrical pumping and suction, and the streamfunctions look extremely similar to the linear (zeroth order) solution.

3.1.2 Regime II: Moderate Ekman Rossby Number

In the second regime the Ekman Rossby number is $R_e < 1$ but is close to 1 (specific values found in table 3.3). For a Rossby number close to 1 we should expect to have more Ekman-nonlinearity playing a role in the approximations. This is seen in figure 3.2. In comparison to figure 3.1, the streamlines are more concentrated near the center in figure 3.2b), and consequently there is a downwelling jet there as well shown in purple with a broader upwelling in green. However the intensity of the upwelling-downwelling asymmetry is not as strong as is seen for $R_e > 1$.

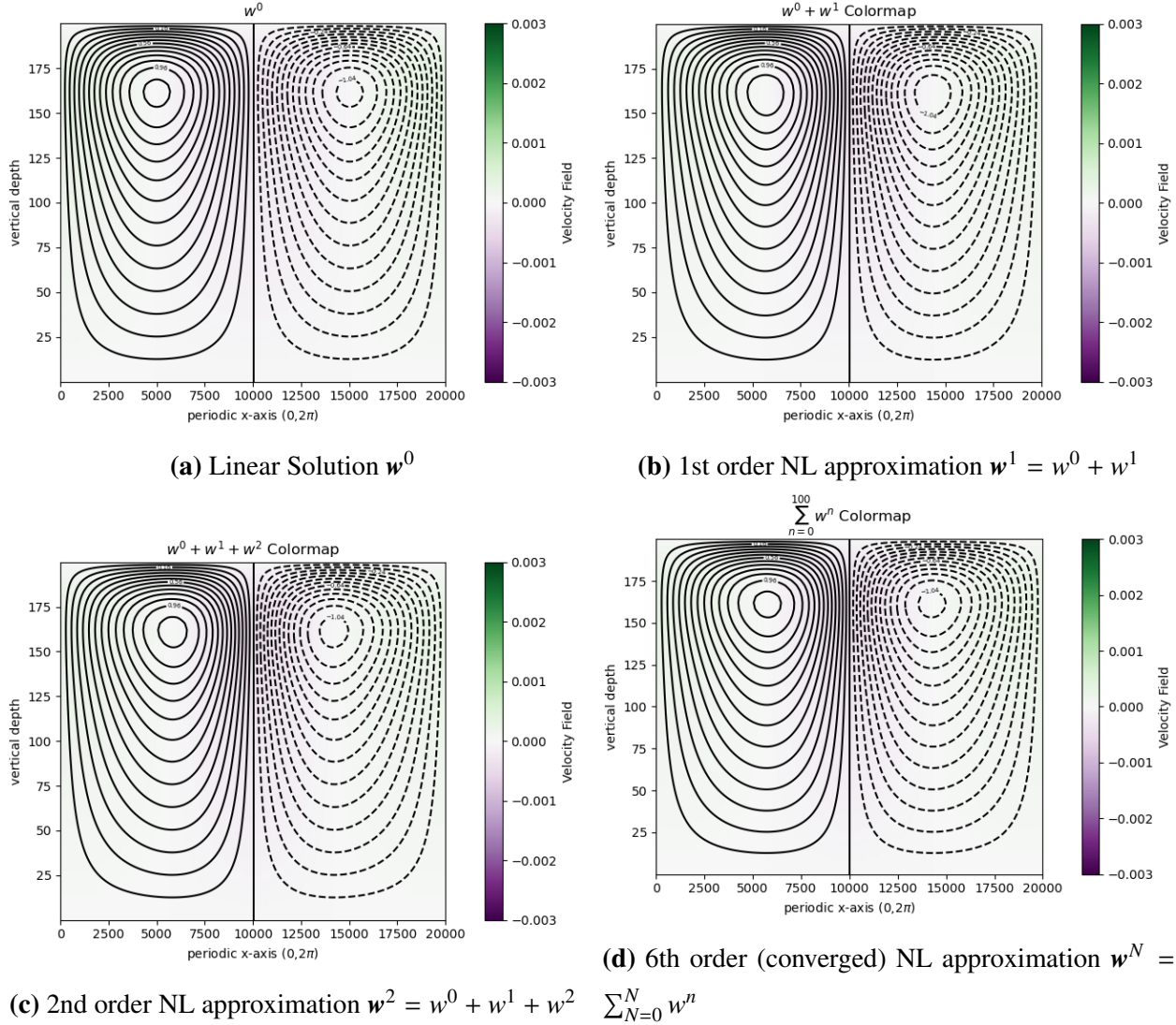


Figure 3.1: Colourmap depicts vertical velocity in the Ekman layer and contour lines represent streamfunction lines. Solutions computed for Regime I where $R_e = 0.2$

3.1.3 Regime III: Large Ekman Rossby Number

In this regime the Ekman-Rossby number is such that $R_e > 1$. Under these conditions we expect to see the effects of significant nonlinearity at play. Specific values for parameters in this regime are found in table 3.4. The resulting state Ψ^{100} , as seen in figure 3.3, shows a much stronger downwelling jet in the center in between the two cells, and a similarly broad upwelling to that of Regime II. This suggests that indeed as the values of R_e increase and go over values of 1 in this model, the intense downwelling and diffuse upwelling asymmetry emerges.

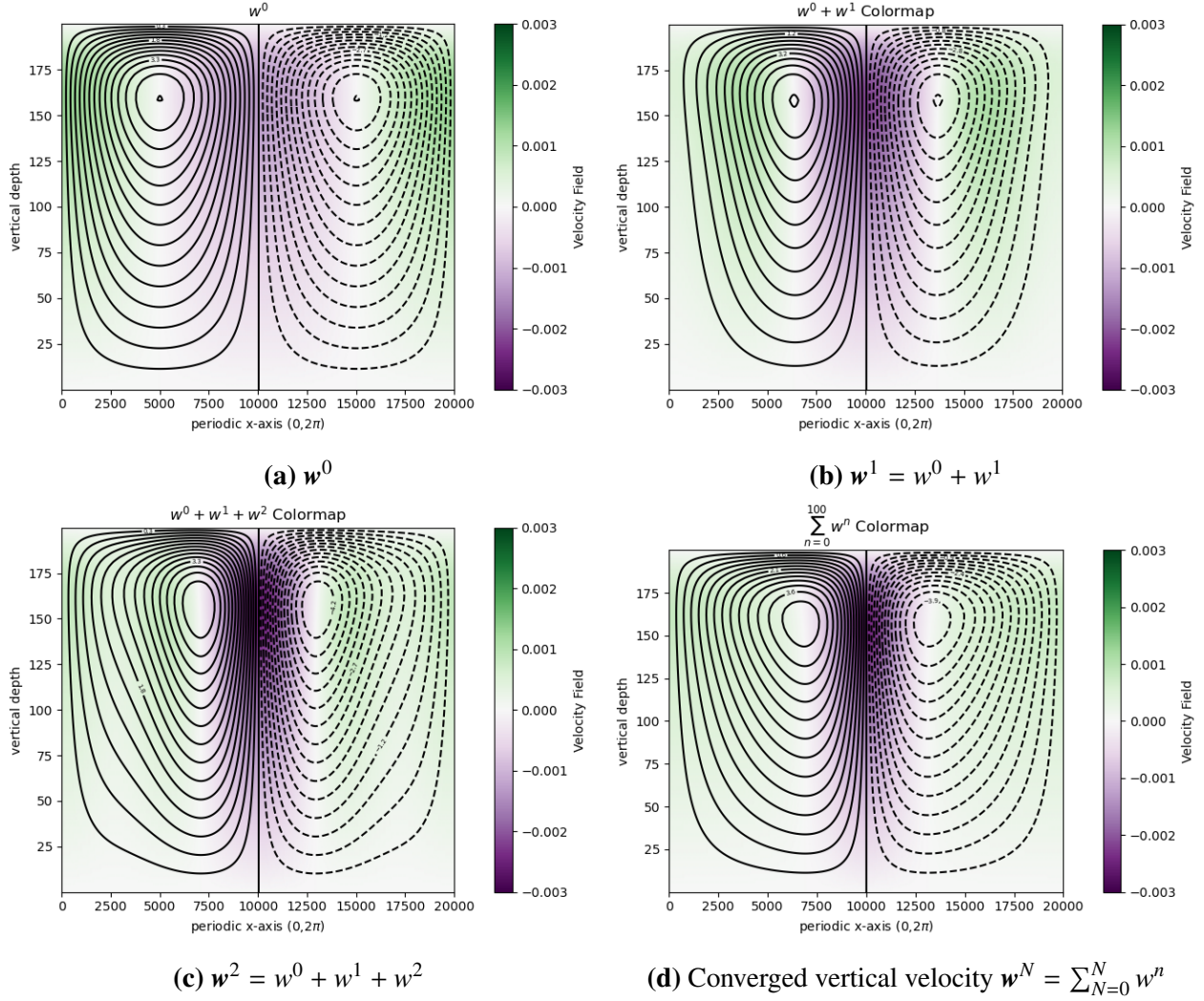


Figure 3.2: Colourmap depicts vertical velocity in the Ekman layer and contour lines represent streamfunction lines. Solutions computed for Regime II where $R_e = 0.9$

In order to address where the asymmetry comes from, we must break down our equations into components we can analyze. For instance, throughout the steady state nonlinear equations, the nonlinear term which we suspect drives asymmetry is composed of a geostrophic and Ekman component:

$$J(\psi, v) = J(\psi, v_g) + J(\psi, v_e) \quad (3.1)$$

Parameter	meaning	value
R_e	Ekman Rossby Number	0.9
R_g	Geostrophic Rossby Number	0.1
A_h	Horizontal viscosity	$2.80 \times 10^2 \text{m}^2/\text{s}$
A_v	Vertical viscosity	$2 \times 10^{-2} \text{m}^2/\text{s}$
r	Damping parameter	9×10^{-5}
f	Coriolis parameter	10^{-4}rads/s
τ_0	Wind Forcing Amplitude	5.73×10^{-4}
N	Max order of approximation	20

Table 3.3: Parameters used in Regime II

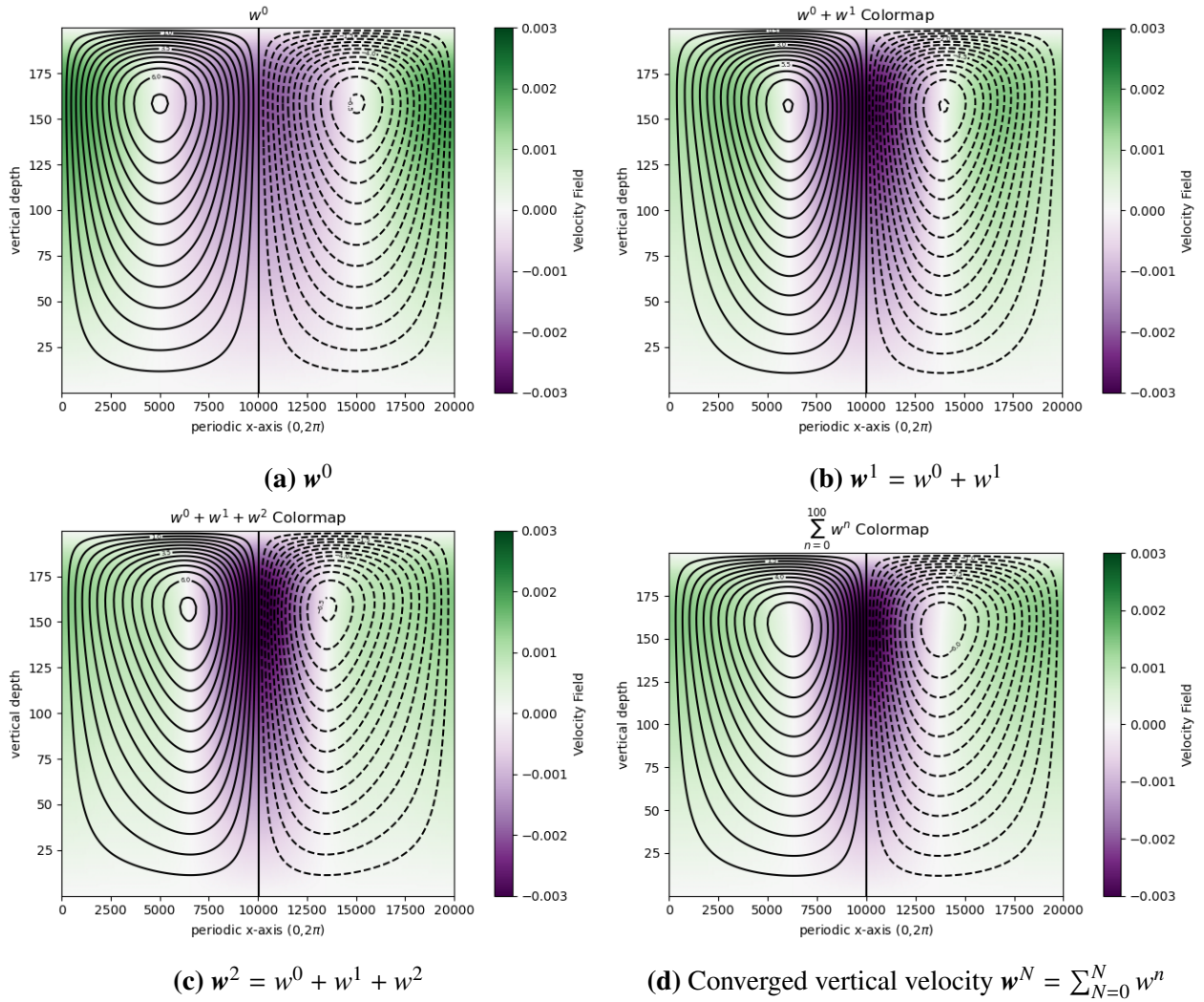


Figure 3.3: Colourmap depicts vertical velocity in the Ekman layer and contour lines represent streamfunction lines. Solutions computed for Regime III where $R_e = 1.75$

Parameter	meaning	value
R_e	Ekman Rossby Number	1.75
R_g	Geostrophic Rossby Number	0.1
A_h	Horizontal viscosity	$5.44 \times 10^2 \text{ m}^2/\text{s}$
A_v	Vertical viscosity	$2 \times 10^{-2} \text{ m}^2/\text{s}$
r	Damping parameter	1.75×10^{-4}
f	Coriolis parameter	10^{-4} rads/s
τ_0	Wind Forcing Amplitude	2.79×10^{-6}
N	Max order of approximation	100

Table 3.4: Parameters used in Regime III

The "classical" nonlinear Ekman theory as discussed in Chapter 1 would consider the nonlinear term to only be $J(\psi, v) = J(\psi, v_g)$ for equation 2.32c where in the expansion of the Jacobian we would obtain Ekman-geostrophic terms which would be considered "nonlinear" in this theory. However what we have done is to also include the $J(\psi, v_e)$ term in the nonlinearity, which is what includes the Ekman-Ekman terms (i.e. Ekman self-advection). We suspect that this is in fact the contribution which primarily drives the characteristic asymmetry we see in higher order solutions. In order to concretely assess this however, we need to explicitly solve the numerical model from Chapter 2 but where Jacobians are now in terms of geostrophic v , and see if any asymmetry arises and to what extent. We do this by simply taking the vertical average of v in our simulation and using that in the Jacobian forcing in the model. Results shown in figure 3.4 indicate no significant difference in the dynamical features or intensity of signals compared to the solutions seen with Ekman-Ekman nonlinearity in figure 3.3. This suggests that the approach of classical nonlinear Ekman theory would be insufficient for seeing this phenomena, as our test shows negligible contribution from the forcing corresponding to only Ekman-geostrophic terms and no Ekman-Ekman terms. To further investigate this we look at the balance in equation 2.32a and test the impact each term has on the forcing of the solution.

In the steady state equations we have a balance of the nonlinearity (Jacobian term) equals $f v_z + F$ where $F = A \nabla^2 \zeta = A_h \zeta_{xx} + A_v \zeta_{zz}$ is the dissipative (friction) term. As seen in figure 3.5, the order of magnitude of values from the dissipative term (figure 3.5a) is the same as that of the Coriolis term (figure 3.5b). These plots summed gives the Jacobian in figure 3.5c, however it is

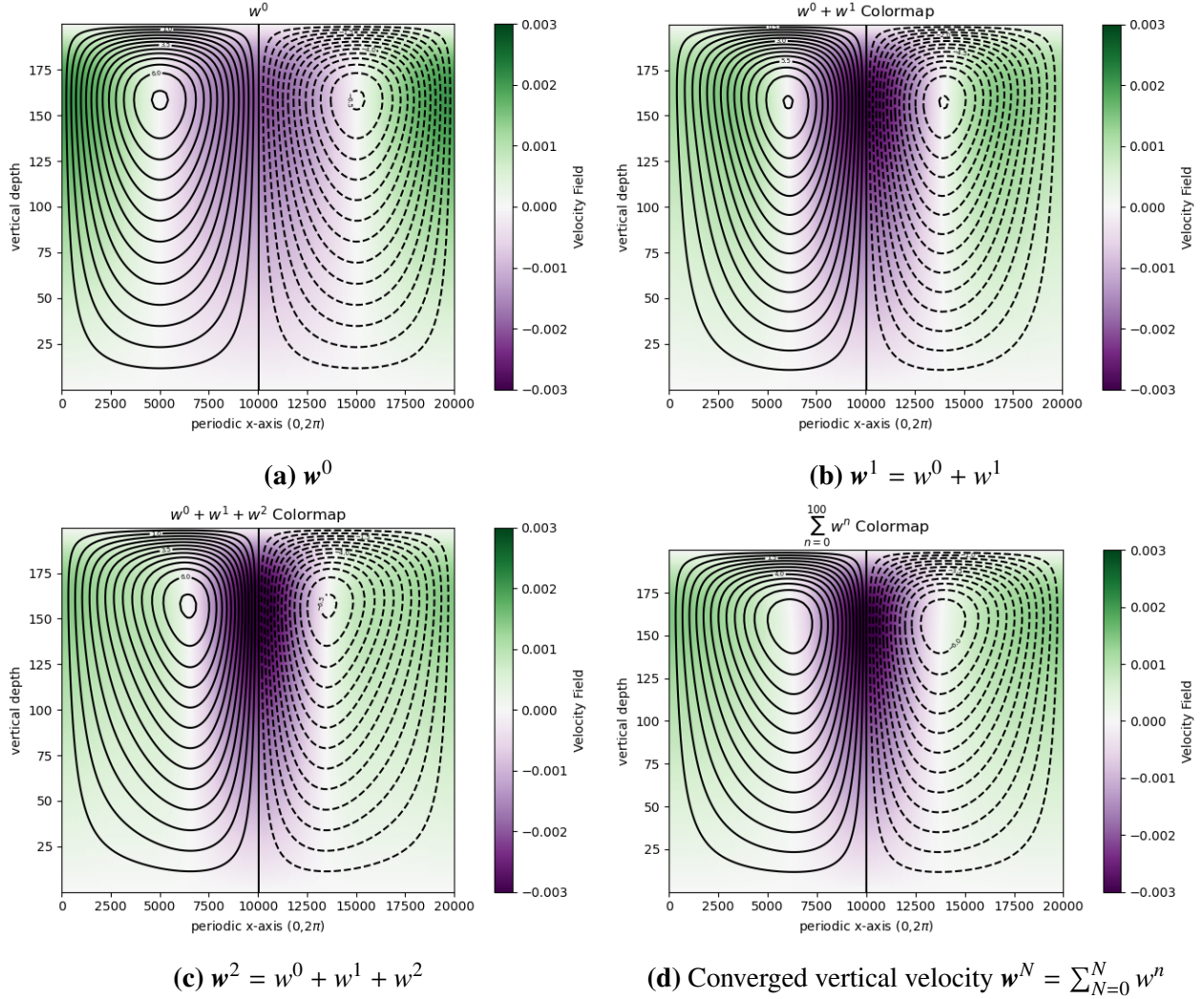
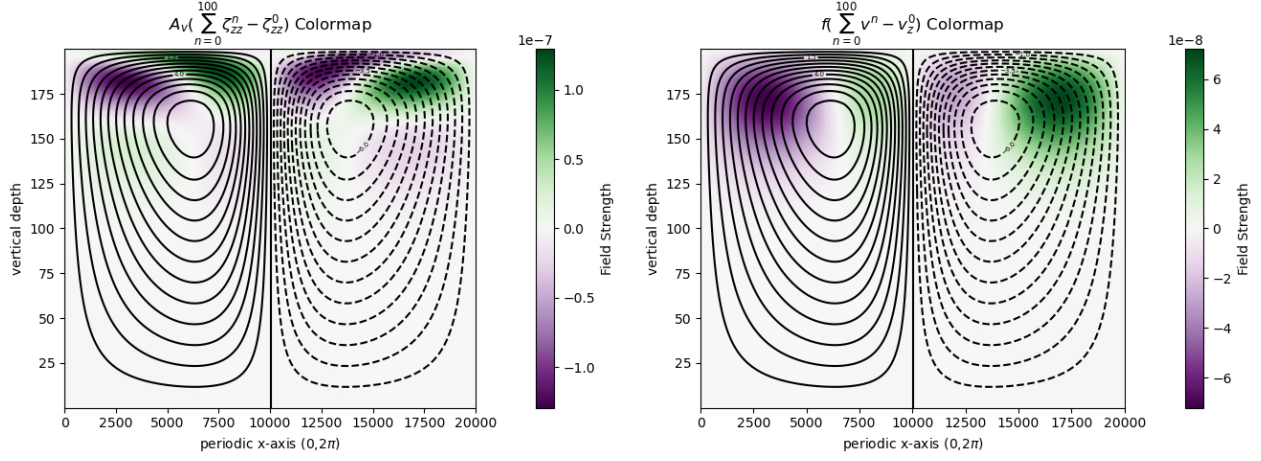


Figure 3.4: Plots for geostrophic forcing where $J(\psi, v_g)$ forces equation 2.32c. Colourmap depicts vertical velocity in the Ekman layer and contour lines represent streamfunction lines. Solutions computed for Regime III where $R_e = 1.75$.

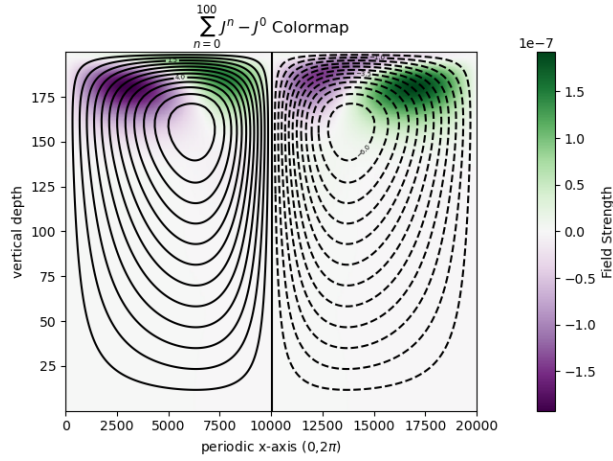
evident that the magnitude of values in figure 3.5c are less than its components, and there is a different placement and shape of cells. This suggests that the signals in $A_v(\zeta_{zz} - \zeta_{zz}^0)$ and $f(v_z - v_z^0)$ significantly cancel each other out in some areas. This is confirmed by comparing the opposite signs in corresponding areas of figure 3.5a) versus b).

If we know how the vorticity comes to be, then we will consequently understand how the asymmetry arises, since it follows that the streamfunction comes from vorticity. Figure 3.6 shows the (nonlinear part of) vorticity, where at first glance it is not evident which term primarily forces



(a) Nonlinear contribution of dissipative term in horizontal vorticity equation

(b) Nonlinear contribution of Coriolis forcing term in horizontal vorticity equation



(c) Jacobian term in Ekman balance

Figure 3.5: Nonlinear component of terms is isolated by subtracting the linear approximation from the n th order approximation

this pattern. Now, we isolate the vorticity due to each term by splitting up the equation as follows:

$$\nabla^2 \zeta = \nabla^2 \zeta_A + \nabla^2 \zeta_B, \quad (3.2)$$

$$\nabla^2 \zeta_A = J(\psi, \zeta), \quad (3.3)$$

$$\nabla^2 \zeta_B = -f v_z, \quad (3.4)$$

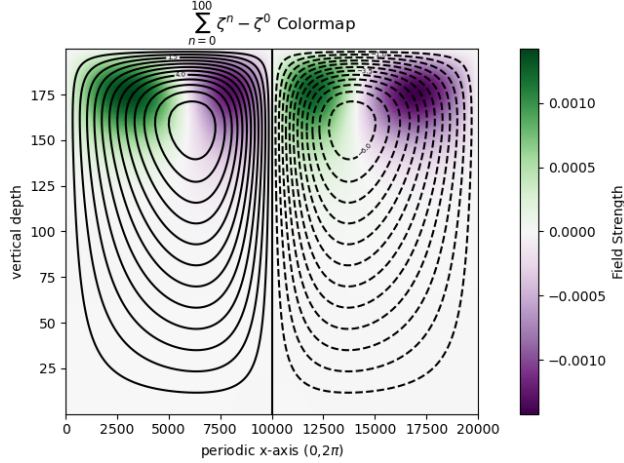


Figure 3.6: Colourmap showing nonlinear contribution to vorticity (ζ minus the linear component (ζ^0)).

where ζ_A is the vorticity driven by $J(\psi, \zeta)$ and ζ_B is driven by $-fv_z$. Now we can treat these as Poisson equations and solve for ζ_A and ζ_B using the already solved variables from the model as input on the RHS of the above equations. The resulting streamfunction and vorticity fields are plotted in figure 3.7. By comparing 3.7a,c to b,d respectively it is evident that the Jacobian forcing is much stronger than that of fv_z . This confirms the hypothesis that it is indeed the nonlinear term mainly contributing to the upwelling-downwelling asymmetry. The corresponding intensities near the central discontinuity are significantly stronger in figures b) and d) where it is forced by the Jacobian. This suggests that self-advection of Ekman terms plays a stronger role in upwelling-downwelling asymmetry than the dissipative fv_z term.

3.2 Parameter Sensitivity

We have seen the clear difference in dynamical features as R_E changes from Regimes I to III, but there are other parameters that the model is particularly sensitive to which have interesting insights to offer. In this section we will briefly overview the sensitivity of the model to a few parameters with interesting results.

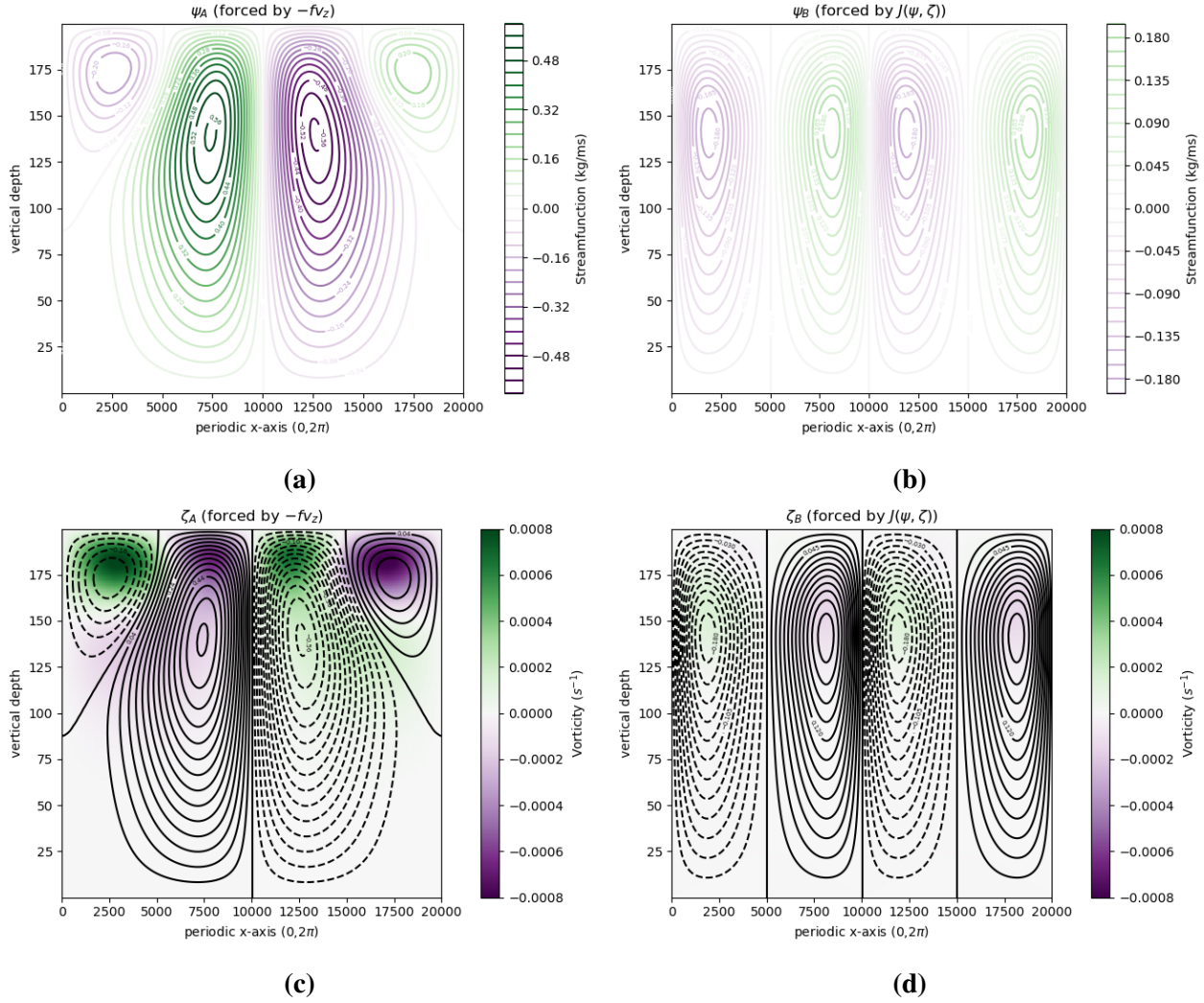


Figure 3.7: Ψ and ζ forced by different terms in horizontal momentum equation. Only NL contributions are plotted (order 0 solution subtracted). Contours correspond to streamfunction Ψ_A and Ψ_B

Horizontal Eddy Viscosity

The convergence of steady solutions are quite sensitive to horizontal viscosity A_h . The greater A_h is, the better the noise is suppressed. The trade-off however, is that as eddy viscosity increases the more interesting features arising from nonlinearity also get suppressed, for instance there is a less narrow downwelling jet that would form. For instance, in the steady model for R_E large, when A_h is increased significantly, solutions converge only after a few orders computed, but the solution looks very similar to the linear ($n=0$) case (see Fig. 3.8).

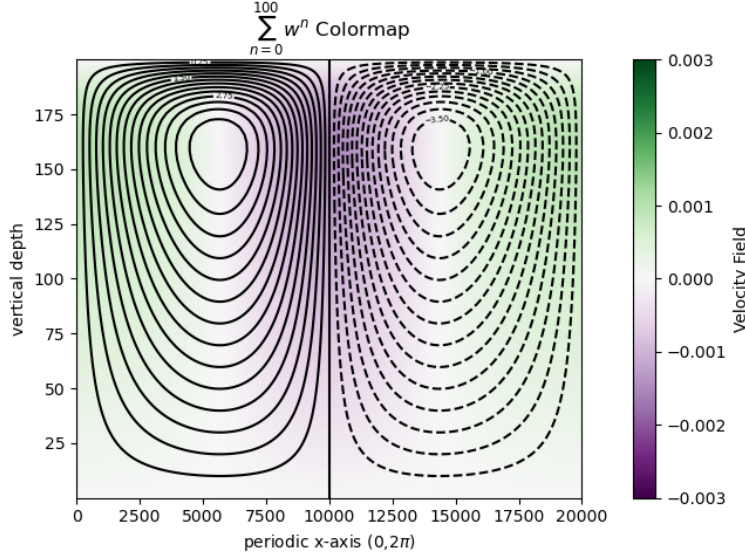


Figure 3.8: $R_E = 1.75$, $A_h = 1.08 \times 10^3 \text{ m}^2/s$, increased horizontal viscosity to exemplify the effect of higher Eddy viscosity while R_E remains the same as before.

Buoyancy

In the case of a weakly stratified ocean where $N = 0.1f$, with all other parameters remaining the same as before, the solutions diverge, as seen in Fig. 3.9 this happens after about order 35.

In order to achieve convergent solutions with $N = 0.1f$, A_h must be increased to $6.5 \times 10^{-2} \text{ m}^2/s$. This, however, decreased the intensity of the downwelling jet, and thus the buoyant case is not largely considered in the scope of this project.

3.3 Time-dependent Solution and Stability Analysis

The time-dependent model is implemented as discussed in section 2.2.4. First it is solved with no additional noise added, to compare it to the steady state solutions. Results are seen in Figure 3.10. In comparison to the streamlines of ψ in the steady solutions (see Fig. 3.3), ψ in the time dependent solutions demonstrate a significantly stronger and more narrow downwelling jet. This is due to the time-dependent solver allowing for smaller values of horizontal Eddy-viscosity A_h (see table 3.5) while producing convergent solutions – whereas the steady solutions had difficulty converging when using smaller values of A_h (see table 3.4).

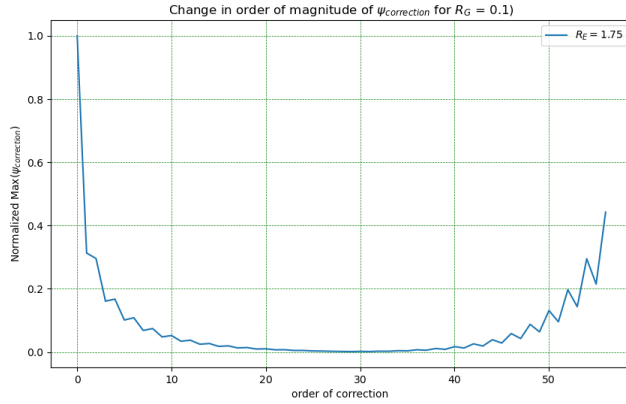


Figure 3.9: Maximum ψ computed in regime with buoyancy flux, showing the divergence of solutions at higher orders of approximation.

Parameter	meaning	value
R_e	Ekman Rossby Number	1.75
R_g	Geostrophic Rossby Number	0.1
A_h	Horizontal viscosity	$1.29 \times 10^4 \text{ m}^2/\text{s}$
r	Damping parameter	$1.75 \times 10^{-4} \text{ m}^2/\text{s}$
f	Coriolis parameter	10^{-4} rads/s
τ_0	Wind Forcing Amplitude	1.11×10^{-3}
t_{stop}	Simulation Duration	0.69 days

Table 3.5: Parameters used in Time-dependent Solution (no noise added)

3.3.1 Stability analysis

Adding a noise function to the initial state of v in the form $\text{pert} = 1e-3 * \text{noise}(zt-z)(z-zb)$ where zt, zb is z at the top and bottom boundary respectively, and noise is a random seeded function. The function is of this form such that the noise is situated away from boundaries. The noise added is seen in Figure 3.11, and the time-dependent solutions with noise are seen in Figure 3.12.

The noise added to v has an order of approximately 10^{-3} while the noise-less v has an order of about 10^{-1} . The noise is significant enough to disturb the solution throughout the 0.69 days the simulation ran, however it appears to stabilize after about 0.6 days (Fig. 3.12d). The same parameters from Regime III were used, however in this simulation it is evident that the downwelling jet is significantly less strong, and thus a less narrow jet. This could perhaps be rectified by decreasing A_h – in which solutions would not converge – or by decreasing the noise added, since the noise-

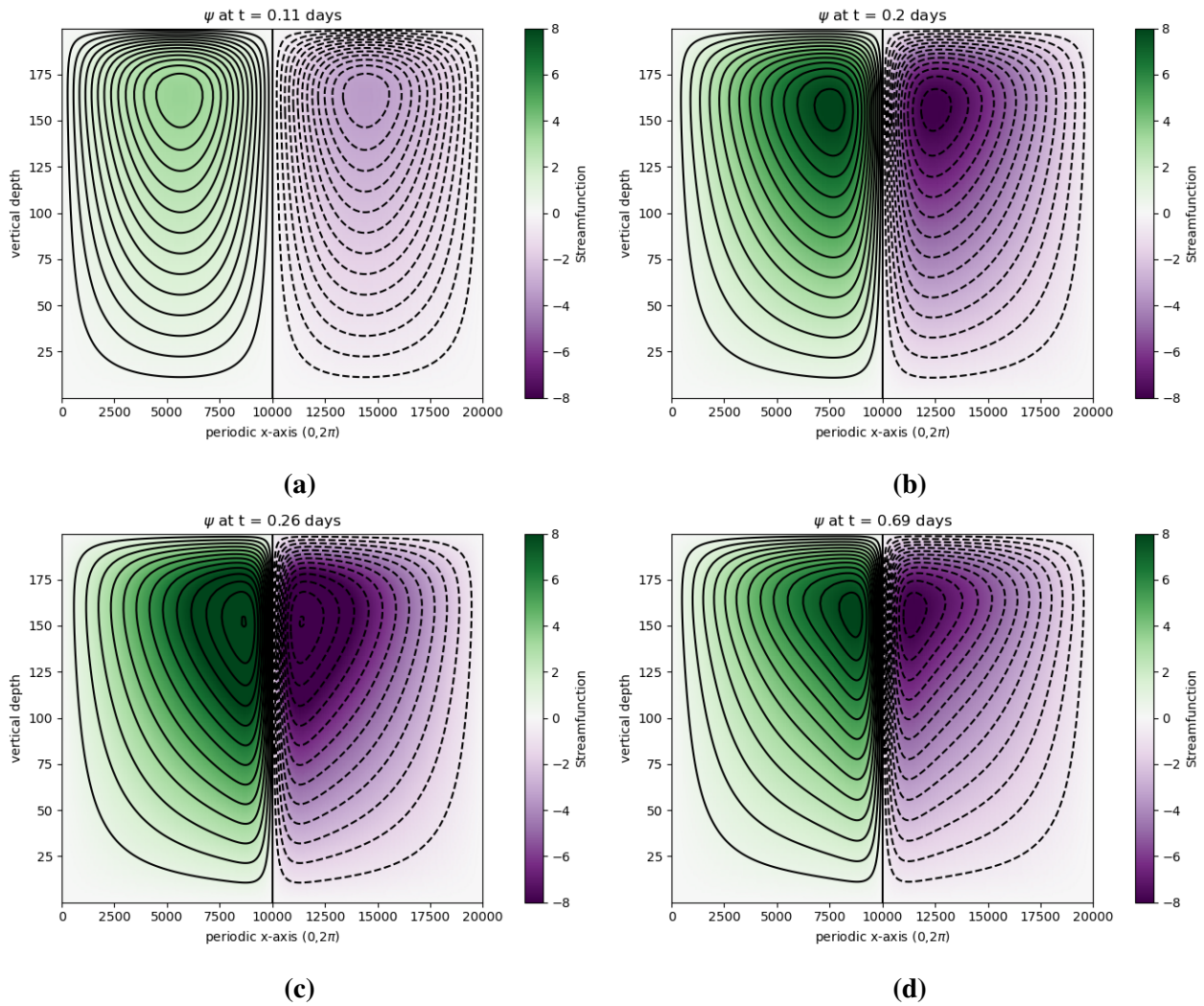


Figure 3.10: Time dependent streamfunction solution at 11th, 71st, 131st and 541st iteration respectively. Simulation ran for a total of 6×10^4 seconds, or approximately 16.7 hours.

less time-dependent solutions appears to have no problem achieving a very strong downwelling jet in the same time-frame of 0.69 days. Alternatively the simulation could be ran for longer than 0.69 days to see if once the solution stabilizes the jet would become more narrow. This was not performed due to constraints in computational cost.

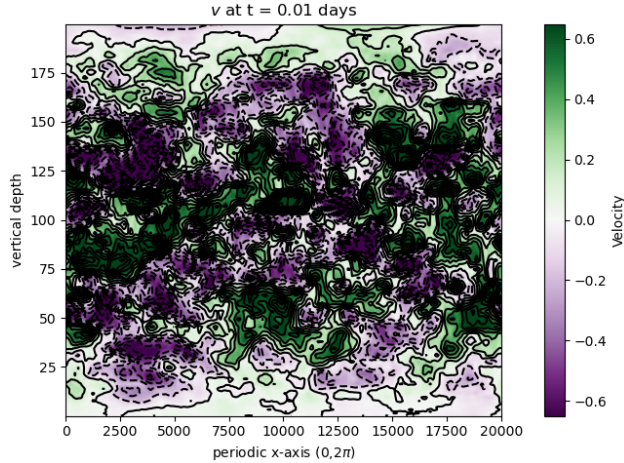


Figure 3.11: Large random background noise added to v at $t = 0$ in the form $1e - 3 * \text{noise}(zt - z)(z - zb)$ where noise is a Python-generated random seeded function.

3.4 Fourier Analysis

Performing a Fourier analysis serves the important role of clarifying the role of higher order corrections to the model. Figure 3.14 is the power spectrum of the different order solutions, comparing the relative amplitude to the number of modes. As we know, with each n^{th} order solution, there are $n + 1$ modes. Therefore, as the order of solution increases so do the number of modes in the solution.

We take the Fourier transform of the streamfunction values at a horizontal slice $z=7\text{m}$, where the strongest values are found by looking at the contour plots. These values are sinusoids pre-Fourier transform, as seen in figure 3.13. Then multiplying the transform by its complex conjugate gives us the energy spectrum as we see in figure 3.14.

We can clearly see the energy containing range, inertial range, then the dissipation range of each order's spectra. As order increases, so does the energy containing range and to some extent the inertial range. Since the energy spectrum depicts the contribution to the energy from each wavenumber, this suggests that as order increases (i.e. wavenumber increases) that those additional wavenumbers contribute significantly to delaying the dissipation of the signal. In other words, this shows the significance of higher order adjustments to the ψ solution with respect to Ekman-Ekman nonlinearity.

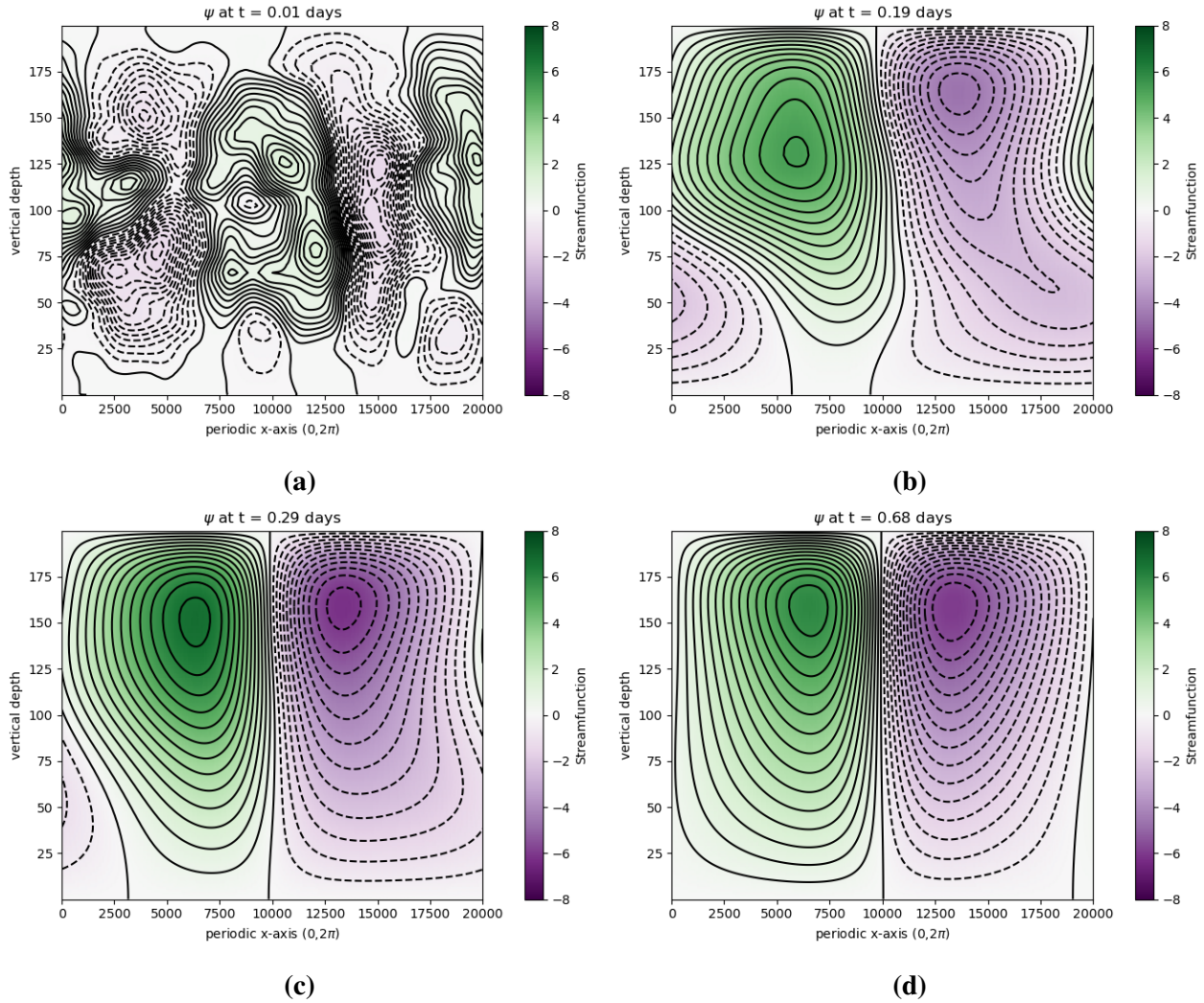


Figure 3.12: Time dependent streamfunction with noise at 1st, 71st, 131st and 411st (final) iteration respectively.

3.5 Conclusions

As we saw in figure 3.3d for $R_e \sim O(1)$, at the 100th order approximation, it clearly depicts a strong downward jet near the center, i.e. the discontinuity, and a diffuse velocity of lesser strength that flows towards to surface. This is precisely the intense downwelling and broad upwelling asymmetry effect that we expected to see at higher order approximations of this model for $R_e \sim O(1)$ with the implementation of Ekman self-advection in the model.

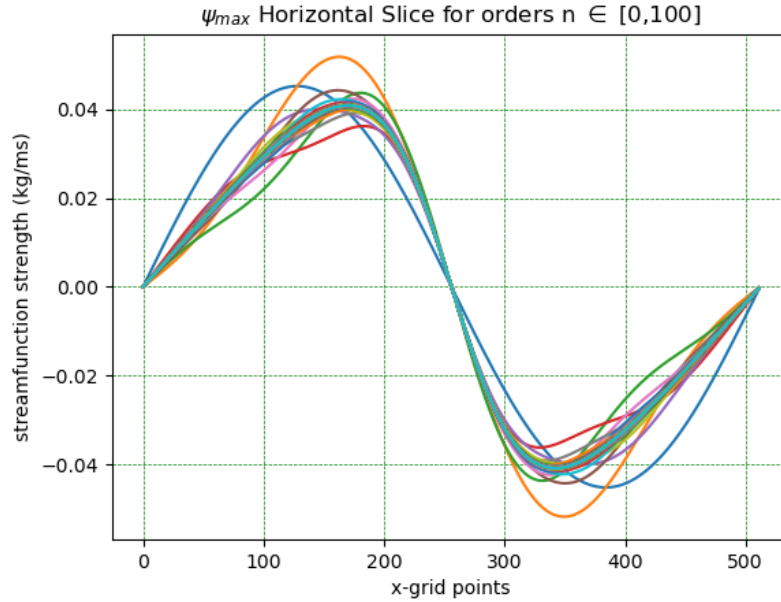


Figure 3.13: The horizontal slice of Ψ^n from Regime III taken at the depth containing maximum streamfunction values, iterated over all orders of correction. This is the signal that we later take the Fourier transform of to analyze.

In order to properly see an even more distinct and concentrated jet and diffuse upwelling like that of [Bourgault et al., 2020], the model would need to be able to take in Rossby numbers much higher than 1, or to be able to decrease A_h without having solutions diverge. An obvious limitation of this study at this stage is the steady model's inability to have solutions for Rossby numbers beyond that of Regime III that do not diverge at high enough order approximations. This is evident by the green line in figure 3.15 corresponding to an attempt to push the Ekman-Rossby number past 1.75 to $R_E = 1.85$. As we can see the higher R_E attempt diverges completely beyond order 30 approximation. In attempts where the model took in different parameters we were able to reach convergent solutions where $R_E > 1.75$, however the parameter changes necessary yielded non insightful solutions. For instance an increase in horizontal viscosity A_h would allow to push to higher Rossby numbers, but then it would create a regime with too much damping and so the nonlinear effects were unevident in the resulting plots (and no upwelling-downwelling asymmetry). Thus, future work involves modifying the methods in the steady model such that a sharper jet can

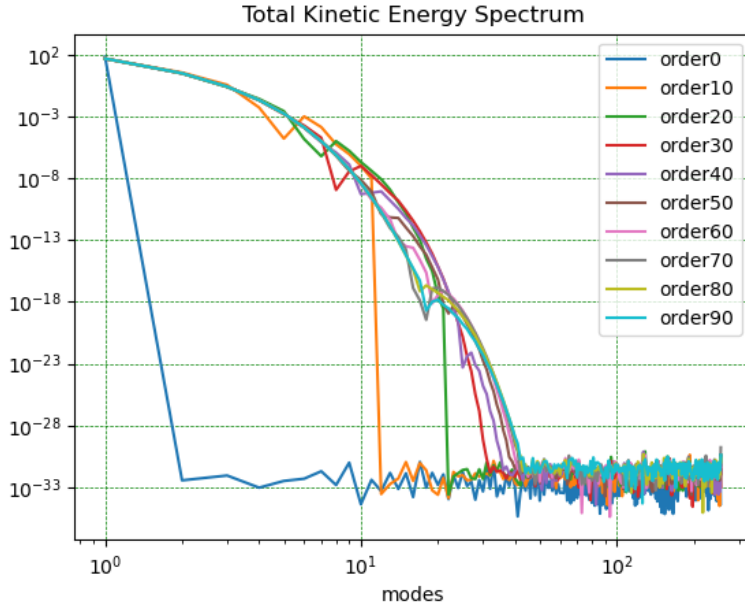


Figure 3.14: Power Spectrum of each 10th order taken of the signal shown in figure 3.13. Plotted on a logarithmic y- and x-axis to show the energy containing range, inertial subrange, and dissipation range.

be found while still having solutions converge, like results seen in the time-dependent model (see Fig. 3.10), although it is currently unknown how this could be done or if it would be possible.

Similarly, testing the model's stability was necessary to assess its robustness. it was performed by solving for the time-dependent version of the model using an iterative time-step scheme. Next steps would include confirming the statistical equilibrium for the time dependent case and repeating a similar forcing analysis to what we have performed, but now we can also add in the Reynolds stress terms and consider transient terms in our analysis. This would mean that our velocity field would look like $\mathbf{u} = \bar{\mathbf{u}} + \mathbf{u}' = \bar{\mathbf{u}}_g + \mathbf{u}'_g + \bar{\mathbf{u}}_e + \mathbf{u}'_e$ where primes denote transient terms.

The future of this work involves incorporating a global climate model (GCM) such as MITgcm to include realistic wind stress coupling as well as sea ice dynamics. This is an important future step because the goal of this research is to ultimately reconcile theory and observations, and a large-ensemble GCM would bring us one step closer to that.

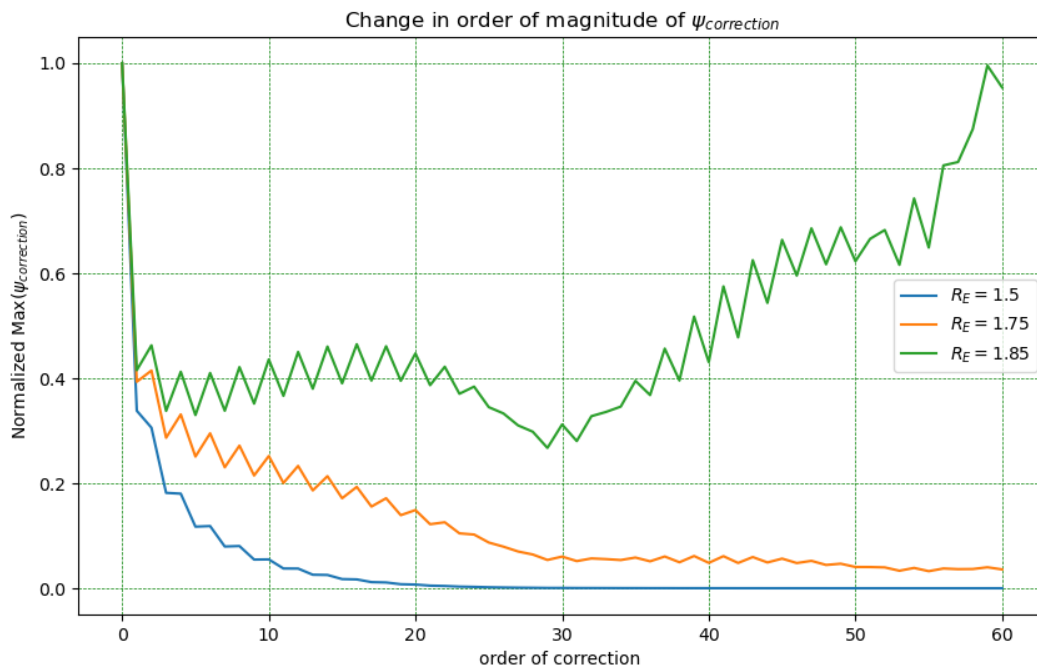


Figure 3.15: The maximum values for streamfunction strength as the order to which Ψ is corrected to (n) increases. Shows that values above $R_E = 1.75$ do not converge. The oscillations in each run is noise from the model “trying” to converge.

Bibliography

- [Bourgault et al., 2020] Bourgault, P., Straub, D., Duquette, K., Nadeau, L.-P., and Tremblay, B. (2020). Vertical heat fluxes beneath idealized sea ice leads in large-eddy simulations: Comparison with observations from the sheba experiment. *Journal of Physical Oceanography*, 50:2189–2202.
- [Burns et al., 2020] Burns, K. J., Vasil, G. M., Oishi, J. S., Lecoanet, D., and Brown, B. P. (2020). Dedalus: A flexible framework for numerical simulations with spectral methods. *Physical Review Research*, 2(2):023068.
- [Chen et al., 2021] Chen, Y., Straub, D., and Nadeau, L.-P. (2021). Interaction of Nonlinear Ekman Pumping, Near-Inertial Oscillations, and Geostrophic Turbulence in an Idealized Coupled Model. *Journal of Physical Oceanography*, 51(3):975–987.
- [Cushman-Roisin and Beckers, 2011] Cushman-Roisin, B. and Beckers, J.-M. (2011). *Introduction to geophysical fluid dynamics: physical and numerical aspects*. Academic press.
- [Duhaut and Straub, 2006] Duhaut, T. H. and Straub, D. N. (2006). Wind stress dependence on ocean surface velocity: Implications for mechanical energy input to ocean circulation. *Journal of Physical Oceanography*, 36(2):202–211.
- [Duquette et al., 2019] Duquette, K., Nadeau, L.-P., Straub, D., Tremblay, B., and Bourgault, P. (2019). Upwelling-downwelling asymmetry of a nonlinear ekman layer. In *22nd Conference on Atmospheric and Oceanic Fluid Dynamics*. AMS.
- [Ekman, 1905] Ekman, V. W. (1905). On the influence of the earth’s rotation on ocean-currents.

- [Hart, 1995] Hart, J. E. (1995). On Nonlinear Ekman Surface-Layer Pumping. *Journal of Physical Oceanography*, 26:1370–1374.
- [Mensa and Timmermans, 2017] Mensa, J. A. and Timmermans, M.-L. (2017). Characterizing the seasonal cycle of upper-ocean flows under multi-year sea ice. *Ocean Modelling*, 113:115–130.
- [Niiler, 1969] Niiler, P. P. (1969). On the Ekman divergence in an oceanic jet. *Journal of Geophysical Research*, 74(28):7048–7052.
- [Salmon, 1998] Salmon, R. (1998). *Lectures on geophysical fluid dynamics*. Oxford University Press.
- [Stern, 1965] Stern, M. E. (1965). Interaction of a uniform wind stress with a geostrophic vortex. *Deep-Sea Research and Oceanographic Abstracts*, 12(3):355–367.
- [Stroeve et al., 2007] Stroeve, J., Holland, M. M., Meier, W., Scambos, T., and Serreze, M. (2007). Arctic sea ice decline: Faster than forecast. *Geophysical research letters*, 34(9).
- [Vallis, 2006] Vallis, G. K. (2006). *Atmospheric and Oceanic Fluid Dynamics*. Cambridge University Press, Cambridge, U.K.
- [Wang and Ruuth, 2008] Wang, D. and Ruuth, S. J. (2008). Variable step-size implicit-explicit linear multistep methods for time-dependent partial differential equations. *Journal of Computational Mathematics*, 26(6):838–855.
- [Wenegrat and Thomas, 2017] Wenegrat, J. O. and Thomas, L. N. (2017). Ekman transport in balanced currents with curvature. *Journal of Physical Oceanography*, 47(5):1189–1203.